Revealing trends and persistent cycles of non-autonomous systems with operator-theoretic techniques: Applications to past and present climate dynamics

Gary Froyland[1,*]**, Dimitrios Giannakis**[2,3]**, Edoardo Luna**[4]**, and Joanna Slawinska**[2]

[1]School of Mathematics and Statistics, University of New South Wales, Sydney, NSW 2052, Australia
[2]Department of Mathematics, Dartmouth College, Hanover, NH 03755, USA
[3]Department of Physics and Astronomy, Dartmouth College, Hanover, NH 03755, USA
[4]Department of Physics, University of Texas at Austin, Austin, TX 78712, USA
[*]g.froyland@unsw.edu.au

ABSTRACT

An important problem in modern applied science is characterizing the behavior of systems with complex internal dynamics subjected to external forcings from their environment. While a great variety of techniques has been developed to analyze such non-autonomous systems, many approaches rely on the availability of ensembles of experiments or simulations in order to generate sufficient information to encapsulate the external forcings, making them unsuitable to study important classes of natural systems where only a single realization is observed. A prominent example is climate dynamics, where an objective identification of signals in the observational record attributable to natural variability and climate change is crucial for making climate projections for the coming decades. Here, we show that operator-theoretic techniques previously developed to identify slowly decaying observables of autonomous dynamical systems provide a powerful means for identifying trends and persistent cycles of non-autonomous systems using data from a *single* trajectory of the system. Using systematic mathematical analysis and prototype examples, we demonstrate that eigenfunctions of Koopman and transfer operators provide coordinates that simultaneously capture nonlinear trends and coherent modes of internal variability. In addition, we apply our framework to two real-world examples from present and past climate dynamics: Variability of sea surface temperature (SST) over the industrial era and the mid-Pleistocene transition (MPT) of Quaternary glaciation cycles. Our results provide a nonparametric representation of SST and surface air temperature (SAT) trends over the industrial era, while also capturing the response of the seasonal precipitation cycle to these trends. In addition, our paleo-climate analysis reveals the dominant glaciation cycles over the past 3 million years and the MPT with a high level of granularity.

Introduction

Operator-theoretic techniques have proven to be highly successful at analyzing dynamical systems[1–3]. These techniques were primarily developed for autonomous dynamics, where the governing rules do not change over time. However, many important phenomena are influenced by changing external factors, resulting in time-dependent governing rules. Examples include collective motion of particles and organisms in response to changes in their environment[4,5], neuronal dynamics under stimuli[6,7], mixing and coherent structure formation under a time-dependent fluid flow[8,9], and the variability of the Earth's climate under natural and anthropogenic forcings[10,11]. In response, at the beginning of the previous decade, extensions

of operator-theoretic techniques to non-autonomous dynamics were developed[12, 13], enabling the analysis of a much wider class of systems. These mathematically rigorous methods only need a single forcing history, but typically require multiple trajectories or multiple observations along the single forcing history.

In recent work[14], the authors developed a framework based on *autonomous* techniques that successfully extracted slowly decaying cycles from a *single nonstationary time series*. Specifically, the El-Niño Southern Oscillation (ENSO)[15] was extracted as a complex eigenvector of the transfer or Koopman operators built from monthly SST images over the past 50 years. Over this time, there is noticeable warming of the ocean, and one could argue that time-dependent techniques should be applied. Nevertheless, the extracted ENSO cycle was in excellent agreement with independent climate observations and displayed greater cyclicity than the corresponding ENSO cycle defined using a standard Niño 3.4 index. We will show in this present work that an estimate of the (non-stationary) Indo-Pacific warming trend, as well as the modulation of the seasonal cycle by the trend, can be obtained through eigenvectors of transfer or Koopman operators. A simple model of this SST increase, combined with oscillatory behavior such as the seasonal cycle or ENSO, is simple harmonic motion with a drift in the mean. We also consider simple harmonic motion with a drift in the amplitude, and simple harmonic motion with a change in the frequency. We will use the latter as a toy model for the Mid-Pleistocene Transition (MPT) of Quaternary glaciation cycles[16], where we will show that transfer/Koopman operators successfully recover the pre- and post-transition cycles from field measurements of benthic δ^{18}O radioisotope concentration[17] (a paleo-proxy for atmospheric CO_2 concentration) as distinct eigenfunctions.

Each of the idealized models studied in this work is nonautonomous. Through these models, we provide theoretical explanations for why autonomous techniques can provide useful information from nonautonomous systems—see Fig. 1 for a schematic illustration of our approach applied to idealized frequency-switching models of the MPT. Our real-world results include reconstructions of surface air temperature (SAT) and precipitation fields using transfer/Koopman eigenfunctions computed from Indo-Pacific SST. These reconstructions reveal regions in South America that have undergone qualitative changes in the phasing and amplitude of the seasonal precipitation cycle over the industrial era. Furthermore, the eigenfunctions computed from δ^{18}O data identify the fundamental 40 kyr and 100 kyr Northern Hemisphere (NH) glaciation cycles over the past 3 Myr and the associated MPT. We find that the 40 kyr cycle and its harmonics persist after the MPT in a low-amplitude state, and the resulting interference with the 100 kyr mode helps explain variations in the amplitude and duration of post-MPT glaciation cycles.

Results

Model classes

Our two main real-world examples are drawn from two single time series: Indo-Pacific SST fields over the industrial era and concentration of benthic δ^{18}O isotopes over the past 3 My. The SST time series incorporates many persistent co-existing cycles of differing frequencies in the subseasonal to interannual band, studied in[14], and a climate change trend, which we address in the present work. The δ^{18}O data has two main frequencies associated with Quaternary glaciation cycles that co-exist for some, but not all, of the time, as well as a nonstationary trend.

We develop idealized models that have these basic types of behavior, namely (i) oscillation with a drift in the mean of the oscillation; (ii) oscillation with a drift in the amplitude of the oscillation; and (iii) a switching between two different oscillations, possibly with co-existence. In each of our real-world examples, it is the underlying dynamics that is undergoing change (e.g., in response to changes in greenhouse gas forcings or orbital forcings of the climate), rather than the measuring device that records the time series. Therefore, we push the time-dependence of the time series into the dynamical system and
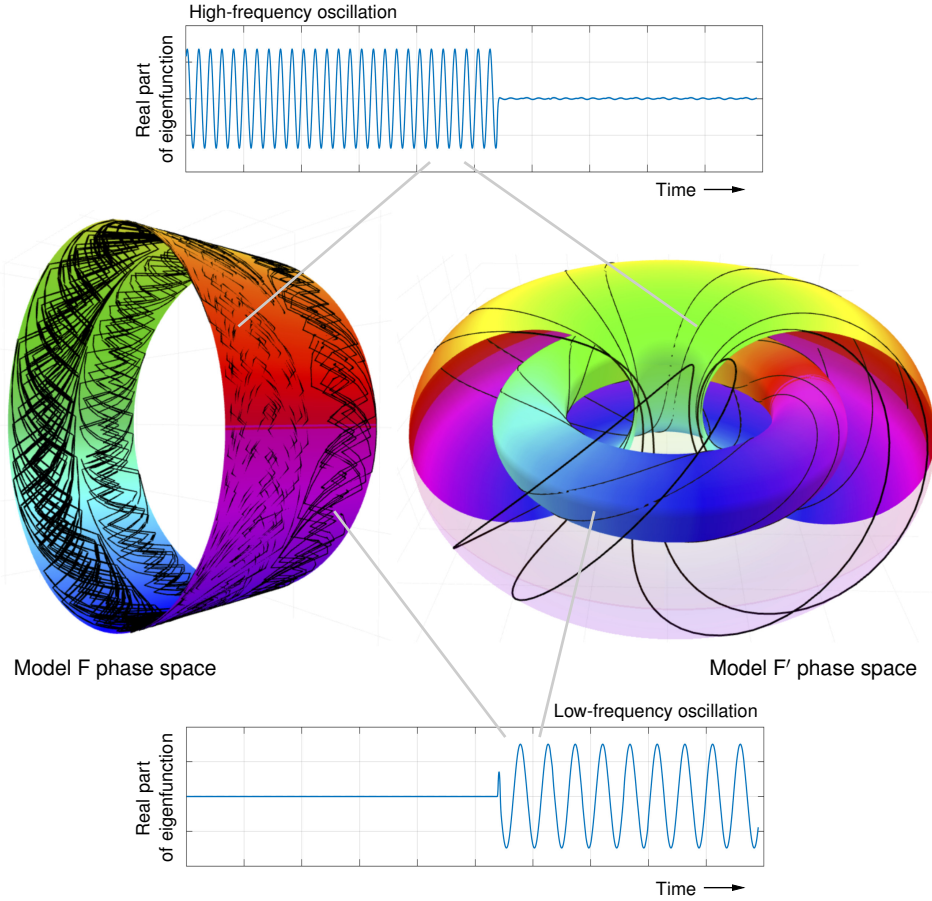
Figure 1. Models of frequency switching (Model F) and co-existing frequencies (Model F′). *Center Left:* The phase space $[0,1] \times S^1$ of Model F (see (2)) is identified with the surface of a cylinder. The (cyclic rainbow) colors represent the scalar output of the observation function $h(\theta) = \cos(\theta)$. The black line represents a trajectory that begins on the left half of the cylinder: the underlying frequency regime parameter $x \in [0,1]$ chaotically evolves on the left of the cylinder (corresponding to $x \in [0,1/2]$), while the oscillation phase θ rotates around the cylinder with a fixed period of 40 time units. At some point, the frequency regime parameter x switches to the right half of the cylinder (corresponding to $x \in [1/2,1]$) and the trajectory thereafter proceeds with a constant rotation rate around the cylinder with a period of 97.35. This switching models the change in glaciation cycle frequency from faster to slower, as observed after the MPT transition period (see section on Quaternary glaciation cycles). The slower oscillation is captured prior to the MPT, while the amplitude of the faster post-MPT oscillation is suppressed. *Upper:* The real part of the second complex eigenfunction for Model F. The slower oscillation is captured after the MPT, while the amplitude of the faster pre-MPT oscillation is suppressed. *Center Right:* The domain $[0,1] \times S^1 \times S^1$ of model F′ (see (6)) is identified with a solid torus, where $x = 0$ corresponds to the outer toral shell and $x = 1$ corresponds to the inner toral shell. The (cyclic rainbow) colors represent the scalar output of the observation function h in (7) on these shells. The black curve represents a trajectory of the system (6) with angular frequencies $\alpha_1 = 2\pi/40$ and $\alpha_2 = 2\pi/97.35$. The trajectory begins on the outer toral shell, where the recorded oscillation of color by the trajectory is relatively rapid. The trajectory then switches the the inner toral shell where the recorded oscillation of color is slower (by a factor α_1/α_2). This switching also models the change in glaciation cycle frequency from faster to slower, and additionally allows for superposition of two frequencies when the trajectory lies between the two toral shells (see equation (7)).
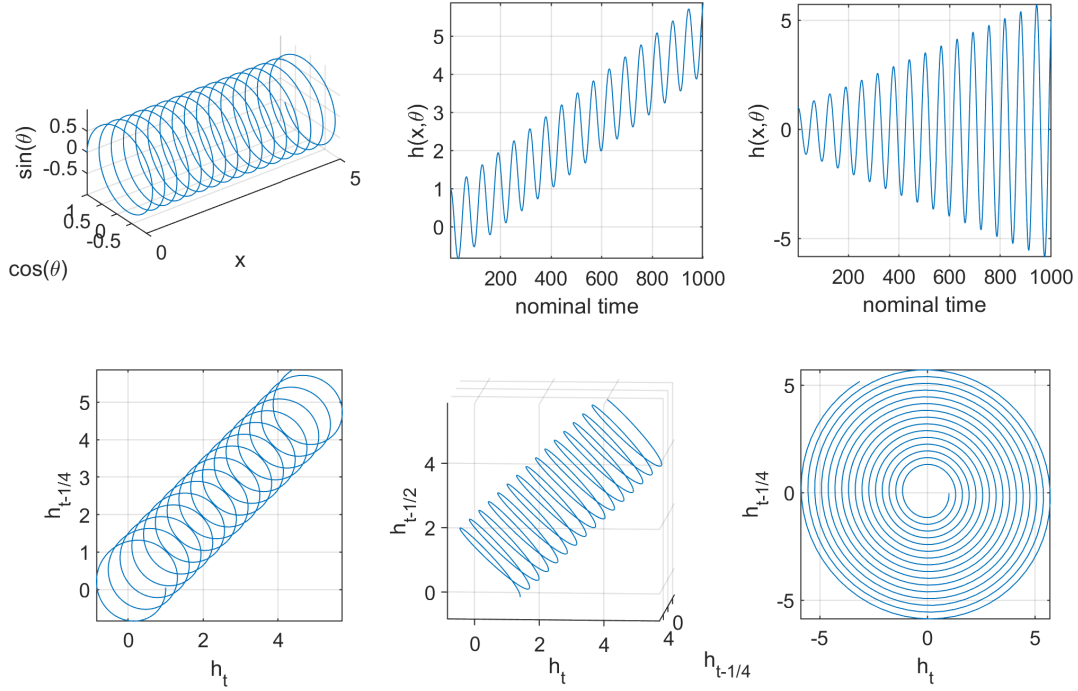
Figure 2. *Upper Left:* A typical trajectory of the (x, θ) coordinates derived from iteration of T in (1), with linear drift $d(t) = t/10$ and $\alpha = 1/10$, and $\tau = 100$. *Upper Center:* Graph of $h(x, \theta) = x + \cos(\theta)$ vs. time, illustrating the creation of a oscillatory signal with a linear drift in the mean of the signal. *Upper Right:* Graph of $h(x, \theta) = (1 + x)\cos(\theta)$ vs. time, illustrating the creation of a oscillatory signal with a linear drift in the amplitude of the signal. Lower Left: Two-dimensional time-delay embedding of the time series $h(x_t)$ shown in Fig. 2 (upper center), using a lag of $1/4$ of the cycle period. Lower Center: Same as Left, but embedded in three dimensions. Lower Right: Two-dimensional time-delay embedding of the time series $h(x_t)$ shown in Fig. 2 (upper right), using a lag of $1/4$ of the cycle period.

keep the observation function time-independent.

Model M: Oscillation with a drift in the mean

A simple dynamical system that incorporates a cycle with a drift transverse to the cycle is helical dynamics around the curved surface of a cylinder. More precisely, we consider the (infinite) cylinder $\mathbb{R} \times S^1$, where S^1 is the circle with unit radius. The notation $T : \Omega \circlearrowleft$ represents a map T from a set Ω into itself. We consider time-dependent dynamics represented by a discrete-time transformation $T : \mathbb{R}^+ \times \mathbb{R} \times S^1 \circlearrowleft$

$$T(t, x, \theta) = (t + 1, x + d(t), \theta + \alpha), \tag{1}$$

where $d(t)$ is a time-dependent drift along the central axis of the cylinder and α is the rate of rotation around the circular base of the cylinder. In this model the coordinate t, representing time, is the driving coordinate. Iterating T for τ iterations, and plotting trajectories of the (x, θ) coordinates on the cylinder embedded in $\mathbb{R}^3$, we obtain a picture such as in Fig. 2 (upper left).

A continuous-time representation of this dynamics is given by the vector field $F : \mathbb{R}^+ \times \mathbb{R} \times S^1 \to \mathbb{R}^3$ defined by $F(t, x, \theta) = (1, d(t), \alpha)$. To create a scalar time series of oscillation with drift, we observe with the time-independent function $h(x, \theta) = x + \cos \theta$, which additively combines the phase of the oscillation θ with the current drift state x to create an oscillation with a drift; see Fig. 2 (upper center).

Model A: Oscillation with a drift in the amplitude

The same dynamical model T in (1) can be used with the altered observation function $h(x, \theta) = (a + x) \cos \theta$, to create an oscillatory time series with an amplitude that varies from a according to the current drift state x. See Fig. 2 (upper right).

Model F: Switching between two different oscillation frequencies

We create a simple class of time-dependent dynamics that can model switching between two distinct oscillations. The state variable x that previously represented the state of the drift will now represent a frequency "regime". This frequency-regime coordinate x is the driving coordinate and evolves according to metastable dynamics, for example according to $f_\delta : [0,1] \circlearrowleft$, for small $\delta > 0$, where

$$f_\delta(x) = \begin{cases} 2x, & 0 \le x < 1/4, \\ \delta + 2(x - 1/4) \pmod 1, & 1/4 \le x < 3/4, \\ 1/2 + 2(x - 3/4), & 3/4 \le x \le 1. \end{cases}$$

The map f_δ is a chaotic map that preserves Lebesgue measure on $[0,1]$. Each of the intervals $[0, 1/2]$ and $[1/2, 1]$ is almost-invariant, and the average probability to switch between these intervals at each iteration is δ. The two intervals will represent two distinct frequency regimes in the angular coordinate introduced below. We consider discrete-time dynamics $T : [0,1] \times S^1 \circlearrowleft$ defined by

$$T(x, \theta) = (f(x), \theta + w(x)\alpha_1 + (1 - w(x))\alpha_2), \tag{2}$$

where $w : [0,1] \to [0,1]$ is a switching function defined by $w(x) = (1 + \tanh(c \cdot (x - 1/2)))/2$, and $c > 0$ is a parameter. For c large (we set $c = 40$ in all of our experiments) $w(x)$ takes values approximately equal to zero on the interval $[0, 1/2)$, and $w(x)$ takes values approximately to 1 on the interval $(1/2, 1]$. Thus, the angular coordinate θ in (2) advances by either α_1 or α_2, depending on the underlying frequency regime controlled by x. Figure 1 (left) illustrates an orbit on the cylinder for the map T; one sees faster rotation around one half of the cylinder in comparison to the other half. To create a time series that switches between the two frequencies, we simply use the (driving-independent) observation function $h(\theta) = \cos \theta$, which records the current phase of the oscillation; see Fig. 6 (upper left).

Why are the outputs of these models idealizations of our data?

Indo-Pacific SST over the industrial era: For Models A and M we imagine that t is time, x is a proxy variable for various greenhouse gas forcings, and that θ is the phase of an oscillatory process such as the seasonal cycle or ENSO. The observation function h is an aggregate quantity (e.g., globally averaged surface-air temperature (SAT) or SST).

δ^{18}**O concentration over the Pleistocene:** For Model F we imagine that x is a proxy variable for CO_2 concentration and regolith deposits, and that θ is the phase of glaciation cycles. Later on we will develop Model F$'$ (see Methods) as an alternative to Model F that is based on two phase angles: θ_1 is the phase of the axial tilt cycle and θ_2 is the phase of the orbital procession/inclination. For both Models F and F$'$ the observation function h outputs the relative concentration of the benthic δ^{18}O isotope.

Time-delay embedding

In practice we imagine that we only have access to a single time series, and that this time series is generated by nonautonomous dynamics with a fixed observation function. A classical approach to such a time series might be to embed it in a higher-dimensional space using Takens' method of delays[18–20]. In this approach, observations h_t with values in $\mathbb{R}^d$ are boosted in dimension through temporal concatenation to produce

a new time series $\mathbf{h}_t := (h_t, h_{t-\ell}, h_{t-2\ell}, \ldots, h_{t-(Q-1)\cdot\ell}) \in \mathbb{R}^{dQ}$, where ℓ is a *lag* and Q is the number of lags. By various types of delay-embedding theorems valid for autonomous[21–23] or nonautonomous[24,25] dynamics, the delay-embedded data can, under appropriate assumptions, faithfully represent the underlying system state even if the observation map h giving the time series data is non-injective.

Yet, even though the original dynamics can be theoretically recovered from observational data, identification of drifts remains notoriously difficult in practice. In this work, we demonstrate that autonomous operator-theoretic methods coupled with delay-embedding can yield useful analyses of nonstationary dynamics. We proceed through the three model classes we have set up in the previous section.

Delay embedding with a drift in the mean and amplitude: Models M & A

Our underlying dynamics is occurring on a helix embedded in $\mathbb{R}^2$ (Fig. 2 (upper left)). Thus, we expect to require at least two embedding dimensions for the scalar signal of h to accurately reconstruct the two-dimensional phase space. Figure 2 (lower left) shows that when the observation h incorporates a drift in the mean, two dimensions are insufficient to uniquely recover the system state; three dimensions (lower center) are sufficient. When the observation function only has drift in the amplitude, two embedding dimensions are sufficient to recover a two-dimensional surface; see Fig. 2 (lower right). Note that the annulus shown in Fig. 2 (lower right) is diffeomorphic to a cylinder.

Delay embedding with oscillation frequency switch: Model F

The switching dynamics given by (2) take place on a cylinder; see Fig. 1 (left). To correctly recover the dynamics we require three embedding dimensions. In the previous subsection, we chose an embedding lag ℓ of 1/4 of the oscillation period. In Model F we have two distinct frequencies, which appear in bursts. Below we will use an abstract result (Lemma 1) to show that with a fixed lag, bursts of *any number of frequencies* may be successfully embedded in three dimensions. This result will also indicate how to best choose a single lag.

Consider a unit circle in the plane, centered at the origin; it has a parametric representation $(x,y) = (\cos(\theta), \sin(\theta)) \in \mathbb{R}^2$. We embed this circle with lagged observation $\cos(\theta)$; i.e., we consider the parametric curve $(\cos(\theta), \cos(\theta+\beta), \cos(\theta+2\beta))$ in $\mathbb{R}^3$ for some lag β and with $\theta \in [0, 2\pi)$. We then have:

Lemma 1. *For each $\beta \in \mathbb{R}$, the parametric curve*

$$\gamma_\beta(\theta) := (\cos(\theta), \cos(\theta+\beta), \cos(\theta+2\beta)), \quad \theta \in [0, 2\pi), \tag{3}$$

is an ellipse embedded in $\mathbb{R}^3$. These ellipses are disjoint for distinct $\beta \in [0, \pi/2)$. When $\beta = \pi/3$ the curves are embedded circles, and the area inside the curves is maximized.

The proof of Lemma 1 is in Methods. Here, we show that the set $\{\gamma_\beta(\theta) : 0 \leq \theta < 2\pi\}$ is an ellipse for each β. Note that the coordinates of $\gamma_\beta(\theta)$ can be written as

$$
\begin{aligned}
(\cos(\theta), &\cos(\theta+\beta), \cos(\theta+2\beta)) \\
&= (\cos(\theta), \cos(\beta)\cos(\theta) - \sin(\beta)\sin(\theta), \cos(2\beta)\cos(\theta) - \sin(2\beta)\sin(\theta)) \\
&= (x, \cos(\beta)x - \sin(\beta)y, \cos(2\beta)x - \sin(2\beta)y),
\end{aligned}
$$

where $x = \cos\theta$ and $y = \sin\theta$. Thus, our delay embedding can be considered as mapping the unit circle linearly via $\Phi : \mathbb{R}^2 \to \mathbb{R}^3$, where

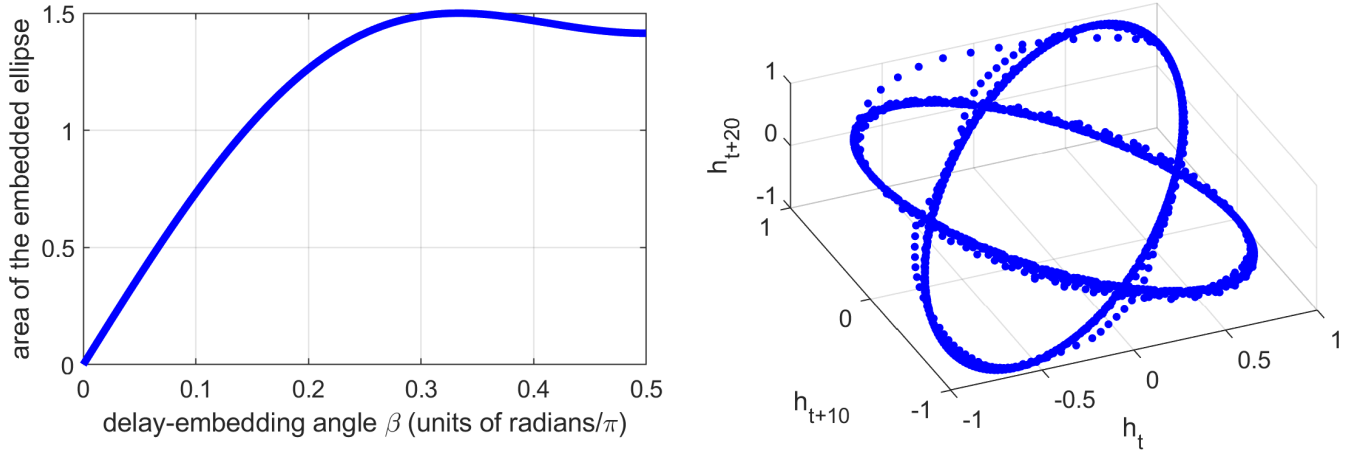$$\Phi(x,y) = (x, \cos(\beta)x - \sin(\beta)y, \cos(2\beta)x - \sin(2\beta)y).$$

Figure 3. *Left:* Area of the embedded ellipse $(\cos(\theta), \cos(\theta + \beta), \cos(\theta + 2\beta))$ as a function of β. *Right:* Embedding of the time series from Model F in Fig. 6 (right) with a lag ℓ of 10 time steps. One obtains two disjoint ellipses of large area that are well separated. The trace joining the ellipses occurs in the short regime where the time series switches between frequencies.

By linearity of Φ, the unit circle in $\mathbb{R}^2$ will be transformed to an ellipse embedded in $\mathbb{R}^3$. Fig. 3 (left) displays the area of the embedded ellipse as a function of β. The region between $\beta = \pi/4$ and $\beta = \pi/2$ is a relative "sweet spot".

We now apply Lemma 1 to our time series with frequency switching generated by Model F. We have two rates of rotation α_1 and α_2, and we therefore generate bursts of samples of single frequencies that look like $\theta = j\alpha_1$ and $\theta = j\alpha_2$, where $j = 0, 1, 2, \ldots$. Suppose that we embedded these bursts with the same lag ℓ in three dimensions; then we obtain chunks of embedding coordinates of the form: $(\cos(j\alpha_1), \cos((j + \ell)\alpha_1), \cos((j + 2\ell)\alpha_1))$ and $(\cos(j\alpha_2), \cos((j + \ell)\alpha_2), \cos((j + 2\ell)\alpha_2))$. We may apply Lemma 1 with $\beta_1 = \ell\alpha_1$ and $\beta_2 = \ell\alpha_2$, to immediately see that these discretely sampled simple harmonic motions with differing frequencies embed in $\mathbb{R}^3$ as *disjoint ellipses*, provided that $0 < \beta_1 \neq \beta_2 \leq \pi/2$. In our example we have $\alpha_1 = 2\pi/40 > \alpha_2 = 2\pi/97.35$, so we set $\ell = 10 \approx (\pi/2)/(2\pi/40)$ in order that the larger angle β_1 hits the outer range of the interval $(0, \pi/2]$. With $\ell = 10$, we then have $\beta_2 = \ell\alpha_2 \approx 0.645$, which yields a large area for the embedded ellipse, as seen in Fig. 3 (left). Figure 3 (right) shows this embedding.

Transfer and Koopman operator computation

Given a dynamical system $T : \Omega \to \Omega$ on a domain Ω and complex-valued function $f : \Omega \to \mathbb{C}$, the transfer operator $\mathscr{L}$ is defined by $\mathscr{L}f = f \circ T^{-1}$, where T^{-1} may be multivalued if T is non-injective. The transfer operator is the natural pushforward action on functions. The Koopman operator is defined as $\mathscr{K}f = f \circ T$, and is the natural pullback on functions. We now describe the construction of transfer operators directly from the embedded time series data. While the approach to numerically constructing the transfer operator is a slight modification of the methodology in[14], we provide a new interpretation of this numerical approximation to explain the form of the eigenfunctions in Models M and A. The time-delay embedding of Models M, A, and F uses scalar outputs $h(x, \theta) \in \mathbb{R}$. Later we will discuss time series observations of SST and δ^{18}O concentration. In the former situation our observations h are vector valued and lie in $\mathbb{R}^d$. As in the case of scalar-valued observations, we time-delay embed these vector-valued observations by concatenation. We obtain a time series of embedded data: $\mathbf{h}_t := (h_t, h_{t-\ell}, h_{t-2\ell}, \ldots, h_{t-(Q-1)\cdot\ell}) \in \mathbb{R}^{dQ}$ for $t = 1, \ldots, N$. For models M, A, and F, we have $d = 1$ and $Q = 3$ and so $\mathbf{h}_t := (h_t, h_{t-\ell}, h_{t-2\ell}) \in \mathbb{R}^3$. We select a forward-step time s (typically corresponding to a single sampling index) and construct a square

array

$$S_{ij} = \exp\left(-\frac{\|\mathbf{h}_i - \mathbf{h}_{j+s}\|^2}{d_i d_{j+s}}\right), \quad i, j = 1, \ldots, N - s, \tag{4}$$

where d_i is the distance from $\mathbf{h}_i$ to its Kth nearest neighbor for modest K. We then row-stochasticize the matrix S to obtain a row-stochastic Markov matrix

$$P_{ij} = S_{ij} / \sum_j S_{ij}. \tag{5}$$

If we think of a vector $\mathbf{f} \in \mathbb{R}^{N-s}$ as values of a function $f : \Omega \to \mathbb{C}$ along our trajectory then the vector $P\mathbf{f}$ corresponds to pushing f forward s steps by $\mathcal{L}^s f$. We will compute eigenvectors v such that $Pv = \lambda v$; in particular, multiplication on the right corresponds to forward evolution in time. We note that by construction $P\mathbf{1} = \mathbf{1}$ (where $\mathbf{1}$ is the N-vector with all entries equal to 1) and thus the leading eigenvalue is 1 and the corresponding eigenvector is constant. We will typically be concerned with the second and lower eigenvalues and eigenvectors.

Note that the matrix S in (4) can be viewed as a non-symmetric discrete heat kernel or non-symmetric diffusion matrix, and the matrix P as the corresponding Markov process. This non-symmetry will be small provided that the step length s is small relative to the length N of the time series. If the bandwidths d_i in (4) are chosen so that the resulting diffusion is commensurate with the advection in embedding space due to the time step s we can expect leading real eigenvalues of P (due primarily to diffusion) to be mixed with leading complex eigenvalues of P (due to periodicities arising from the advective components).

Eigenfunctions for Model M

Figure 2 (upper center) showed an oscillatory time series with a linear drift in the mean of the oscillation. Figure 2 (lower center) showed a three-dimensional embedding of these observations, reproducing a diffeomorphic copy of the original dynamical system shown in Fig. 2 (upper left). We now build a transfer operator approximation on the embedded time series data in Fig. 2 (lower center), according to equations (4) and (5) with $s = 1$ and $K = 7$. Figure 4 (upper row) displays different views of the second eigenvector v_2 with eigenvalue $\lambda_2 = 0.9943$. On the left is the original time series, colored by the value of v_2. In the center is the value of $v_{2,t}$ plotted against time index t. The key point is that we see qualitative agreement in the behavior of the eigenvector value versus time (center) and the mean value of the drift (left). At the right is the embedded time series, colored by the value of v_2.

We remarked above that the matrix P can be seen as an approximation of a slightly biased Markov diffusion process on the spiral structure. The slight bias is due to the the forward-step time $s = 1$ rather than $s = 0$, which would be unbiased. The second eigenvector of such a diffusion process is consistent with the upper-right panel of Fig. 4. Thus the underlying reason why Fig. 4 is colored from one end of the helix to the other is that P represents a slightly biased random walk along the one-dimensional spiral.

Focusing now on the lower row of Fig. 4, in the left panel we construct an asymmetric quadratic drift in the mean of the oscillation. We compute v_2 (with eigenvalue $\lambda_2 = 0.9984$) using the corresponding three-dimensional embedding shown in the lower-right panel as the basis for constructing the matrix P. In the center panel of the lower row of Fig. 4 we see that the eigenvector value versus time qualitatively reflects the drift in the mean of the oscillatory signal in the left panel. The reason for this correspondence is the same as for the linear drift, but slightly more complicated because of the non-monotonicity of the drift. In the embedded space in the lower-right panel of Fig. 4 we see that the embedded signal doubles back over itself. We may again consider P has approximating a slightly biased Markov diffusion process on the structure in the lower-right panel of Fig. 4. The eigenvector values appear as they do because of the geometric proximity of different parts of the embedded time series.
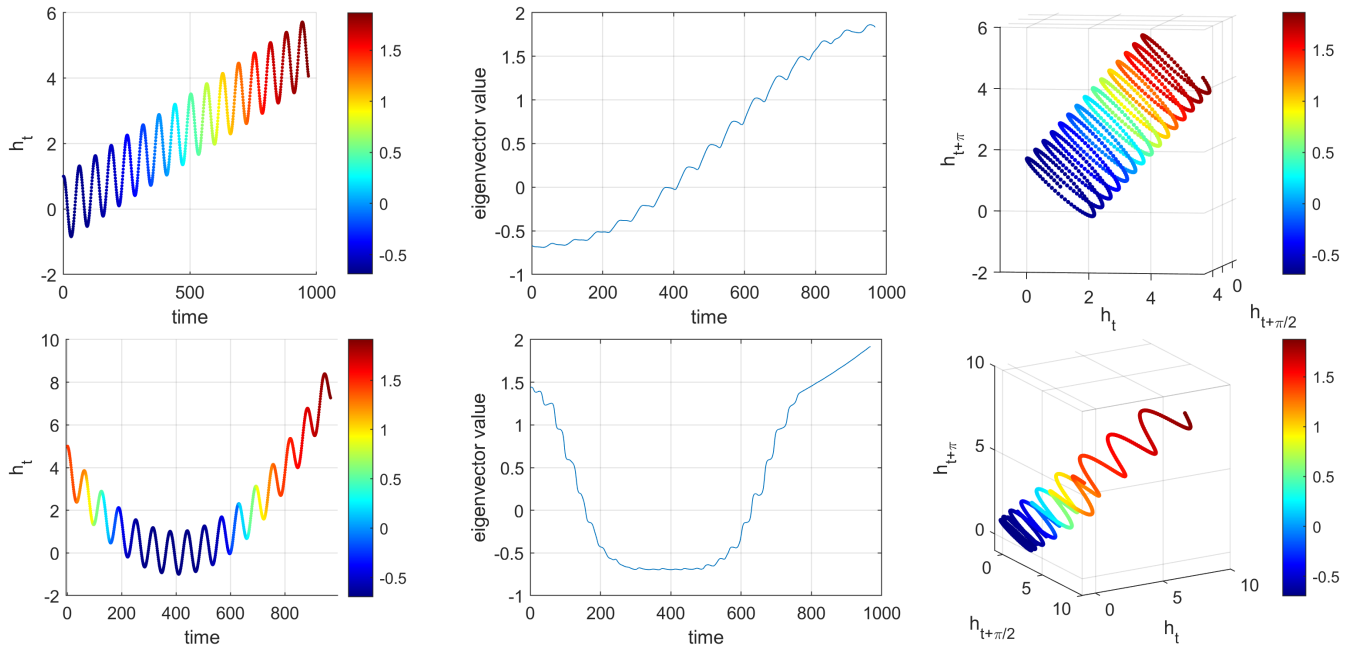
Figure 4. *Upper:* Linear drift. The left panel shows the raw time series vs. time, colored according to the first nontrivial real eigenvector (second in the global ordering v_2); center panel shows the second eigenvector value vs. time; right panel shows the embedded data colored according to v_2. *Lower:* Non-monotonic quadratic drift. The left, center, and right panels show analogous objects as for linear drift.

Eigenfunctions for Model A

In the upper row of Fig. 5 we show (left to right): (i) a time series with linear drift in the amplitude; (ii) the values of the leading nontrivial real eigenvector (v_4) versus time; and (iii) the two-dimensional embedded time series colored according to the values of v_4. All computations were made with $s = 1$ and $K = 7$. The second and third eigenvalues are a complex-conjugate pair $0.9891 \pm 0.0991i$ corresponding a rotation of 0.0998 radians per time step, which is almost exactly the rotation rate of $\alpha = 1/10$ noted in Fig. 2. We are interested in extracting the drift in the amplitude and we move on to the first nontrivial real eigenvalue, which appears in position 4: $\lambda_4 = 0.9825$. This eigenvalue is real because there is no oscillation associated with the drift in the amplitude. The embedded points in the upper-right panel of Fig. 5 are colored from "inside to out" because we may again interpret P as a slightly biased approximate Markov diffusion process. In particular, the upper-center panel qualitatively extracts the increasing amplitude.

The lower-left panel of Fig. 5 shows a more complicated non-monotonic quadratic amplitude variation. This variation is captured in the lower-center panel from the leading nontrivial real eigenvector v_6, for the same reasons as those given above, namely the geometry of the embedding drives the form of the eigenvector.

Eigenfunctions for Model F

We return to the time series in the upper-left panel of Fig. 6. This time series is embedded as in Fig. 3 (right), leading to two ellipses that are disconnected, apart from the short trajectory joining them. We construct the matrix P as above with $s = 1$, but we increase K to 25 in order to achieve a robust numerical solution for the eigenvectors. We find that eigenvalues 2 and 3 are a complex-conjugate pair with $\lambda_2 = 0.9866 + 0.1547i$ and eigenvalues 4 and 5 are another complex-conjugate pair with $\lambda_4 = 0.9954 + 0.0660i$. The arguments of these complex eigenvalues correspond to rotation periods of 40.39 and 94.95 time units, which compare
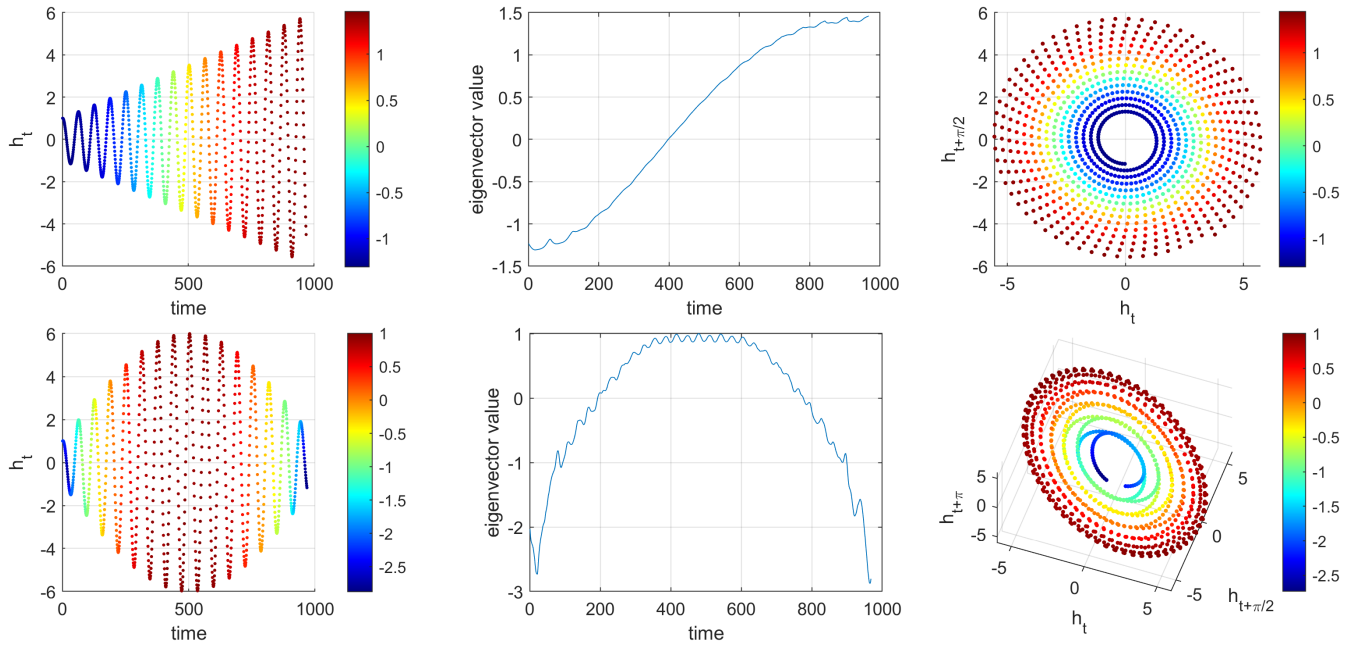
Figure 5. *Upper:* Linear drift. The left panel shows the raw time series vs. time, colored according to the first nontrivial real eigenvector (fourth in the global ordering v_4); center panel shows the second eigenvector value vs. time; right panel shows the embedded data colored according to v_4. *Lower:* Non-monotonic quadratic drift. The left, center, and right panels show analogous objects as for linear drift. The vector shown is again the first nontrivial real eigenvector (sixth in the global ordering v_6).

to exact values of 40 and 97.3537.

The corresponding eigenvectors are shown in Fig. 6.

In the left panels of Fig. 6 we see the original time series (upper), the real parts of the leading complex eigenvector versus time (center), and the real parts of the second complex eigenvector versus time (lower). The embedded time series data colored according to the real parts of the two complex eigenvectors is shown in the right panels. In particular, we note that the oscillation period in the second half of the center left panel is identical to the oscillation period in the second half of the upper-left panel (the original time series), while the amplitude in the first half of the time series is suppressed in the eigenvector values (center left). In this sense, the leading complex eigenvector has *extracted the cycle that is supported on the second half of the time series*.

Similarly, in the lower-left panel of Fig. 6 we see that the large amplitude is concentrated in the first half of the time span and that the oscillation period is nearly identical to the oscillation period of the corresponding second half of the original time series (upper left). This first half of the eigenvector corresponds to one of the two ellipses in the right-most panel. Thus, the second complex eigenvector has extracted the second frequency in the time series. Overall, the two leading complex eigenvectors have *identified and filtered the distinct frequencies of the original signal*.

The reason why the eigenvectors of P behave in this way is analogous to our discussion with the drift in the mean and amplitude. The geometry of the embedded time series again plays a key role. In this case, we have two ellipses that – apart from some small regions – are disconnected from one another. If we had two completely disconnected ellipses we should obtain two complex-conjugate eigenvalue pairs describing the rotation frequency for each ellipse; see[14] for details. In the present setting, the embedded time series is slightly perturbed from this idealized situation, and we therefore obtain eigenvectors that are
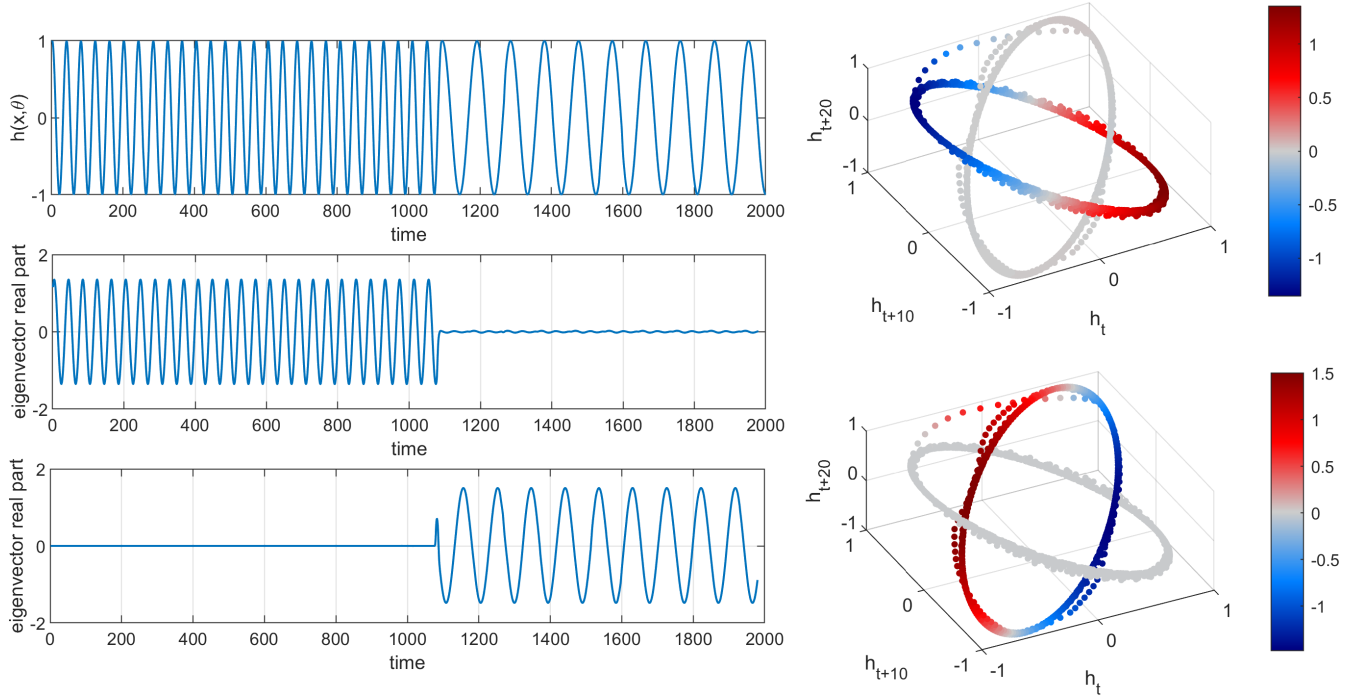
Figure 6. Separation of the two distinct frequencies in Model F by two complex eigenvectors of the approximate transfer operator P. Model F is defined in (2) with $\delta = 7.5 \times 10^{-4}$, $\alpha_1 = 1/40$, and $\alpha_2 = 1/97.3537 \approx 1/100$. *Upper Left:* Graph of observation function $h(x, \theta) = \cos(2\pi\theta)$ vs. time, illustrating the creation of an oscillatory signal switching between two frequencies. *Center Left:* The real part of the first complex eigenvector vs. time. *Lower Left:* The real part of the second complex eigenvector vs. time. *Upper Right:* the three-dimensional embedding of the time series, colored by the real part of the first complex eigenvector. Lower right: As for the upper right, but with the second complex eigenvector.

a slight perturbation of the eigenvectors in the idealized situation.

Climate variability and trends over the industrial era

One of the key challenges in advancing our scientific understanding of climate dynamics and improving the skill of climate forecasts and projections is to objectively identify the fundamental modes of climate variability, operating on timescales spanning months (seasonal cycle) to decades (low-frequency oceanic variability) under the influence of time-dependent natural and anthropogenic external forcings[26–28]. When analyzing observational data, we sample a single dynamical trajectory through observational networks with time-dependent biases, making the task of delineating natural variability from forced response particularly challenging[29, 30].

As noted in the Introduction, previous work[14] has shown that operator-theoretic techniques successfully extract fundamental cycles of climate dynamics such as ENSO, the seasonal cycle, and combination modes between ENSO and the seasonal cycle[31] from monthly-averaged SST snapshots, despite the presence of a nonstationary climate-change trend in the data and the fact that the analysis techniques were originally designed for autonomous dynamics. In addition, the transfer/Koopman operator spectral decompositions yield eigenfunctions with nonstationary associated time series that are broadly consistent with accepted climate change signals over the satellite era[32]. The spectra also contain "trend combination modes" corresponding to products between the trend and seasonal cycle eigenfunctions. Building upon the

idealized models described in the preceding sections, in this section we extend the analysis of ref.[14] to a ~ 130 yr interval spanning the industrial era.

Dataset and analysis description

We analyze monthly-averaged SST fields with a $2°$ resolution from the ERSSTv4 reanalysis product[33] on the Indo-Pacific domain 28°E–70°W, 60°S–20°N. In addition, we analyze monthly-averaged, $5°$ global surface air temperature (SAT) anomaly data from the NOAA Global Surface Temperature Dataset (NOAAGlobalTemp), Version 5.0[34], and monthly-averaged, $1°$ global precipitation data from the NOAA/CIRES/DOE 20th Century Reanalysis version 3 (20CRv3)[35]. This analysis interval is longer than the 1970–2019 interval studied in ref.[14] as the focus of this paper is on long-term climate change trends which are more significant over our analysis period that covers a significant portion of the industrial era.

We extract eigenfunctions v_j from the SST data using the kernel-based approach for approximating the generator of the Koopman/transfer operator groups described in ref.[14]. Note that the SAT and precipitation fields are not employed in our eigenfunction computations—we use these fields instead as target variables for reconstruction based on our eigenfunctions. Additional details on the operator and reconstruction calculations are provided in Methods. Supplementary Fig. 1 displays the spectrum of the generator, where the real and imaginary parts of the eigenvalues represent growth rate and oscillatory frequency, respectively. The eigenvalues can be grouped into families associated with the seasonal cycle, ENSO, trends, and decadal variability, similarly to ref.[14]. In this paper, we will focus on the trend and seasonal-cycle modes. Note that each eigenfunction v_j has a corresponding eigenfrequency $\omega_j \in \mathbb{R}$ and an eigenperiod $T_j = 2\pi/\omega_j$.

Revealing climate change trends through eigenfunctions

Figure 7(a, d) displays time series of eigenfunction v_6 of the generator along with globally averaged SST (Fig. 7(a)) and SAT (Fig. 7(b)) anomalies computed relative to a 1971–2000 monthly climatology. It is evident that v_6 represents a nonstationary pattern that correlates positively and significantly with the evolution of globally-averaged SST and SAT on decadal timescales. Notable features of the v_6 evolution include a modest amount of cooling over the first decade of the 20th century, followed by a warming episode from the mid-1930s to the late 1940s and a period of more sustained warming starting in the 1950s and lasting through the end of the analysis interval. This latter period is marked by episodes of rapid warming such as 1975–1980 and 2013-2018, but also contains intervals of warming slowdown, including the apparent warming "hiatus" that took place in the first decade of the 21st century. An analogous set of computations were made by estimating the transfer operator $\mathscr{L}$ of six-monthly evolution of SST anomaly fields. The second eigenvector (the leading nontrivial eigenvector) extracts the warming trend; see Supplementary Note 1 and Supplementary Fig. 2 for details. The features mentioned above are broadly consistent with accepted climate change trends over the industrial era[28–30], and demonstrate the capability of autonomous operator-theoretic techniques to provide nonparametric representations of nonstationary signals generated by non-autonomous dynamical systems.

Next, we consider spatial visualizations of the SST and SAT trends associated with v_6 obtained from the reconstruction procedure described in Methods. This procedure is closely related to the reconstruction methods employed in extended empirical orthogonal function (EEOF) analysis and singular spectrum analysis (SSA)[36], and in essence involves projecting a target observable of interest to the cyclic subspace generated by a collection of one or more approximate Koopman/transfer operator eigenfunctions. In Fig. 7(b, c) we show snapshots of reconstructed global SST anomalies obtained from v_6 for January 1919 and 2019, respectively; Fig. 7(e,f) shows the corresponding patterns of global SAT anomalies. These patterns capture the climate warming that has taken place over industrial era, particularly over Arctic land
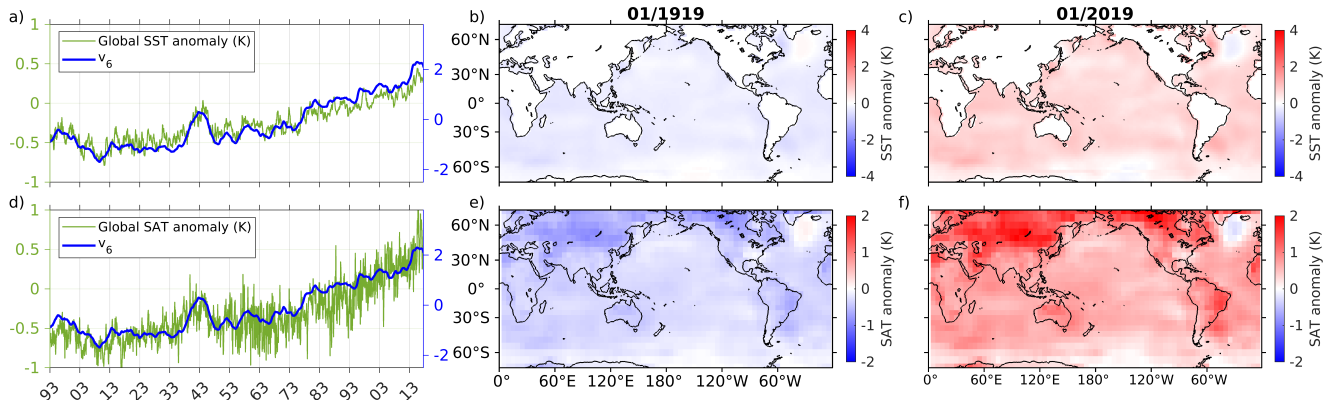
Figure 7. Reconstruction of SST and SAT trends over the industrial era using eigenfunction v_6 of the generator. Panels (a, d) show time series of globally averaged SST and SAT anomalies, respectively, along with time series of v_6. Panels (b, c) show global spatial maps of SST anomalies for January 1919 and 2019, respectively. Panels (e, f) show global SAT anomalies for the same dates.

masses (see Fig. 7(f)). Finer-grained features, such as atmospheric cooling in the Northeast Atlantic and Antarctic Peninsula are also clearly visible.

Response of seasonal cycle of precipitation to climate change

The seasonal cycle of the Earth's climate is driven by periodic variations of solar insolation between the northern and southern hemispheres over each year. The response of climatic variables to this driving depends on many factors and varies significantly between regions, even at the same latitude. In subtropical regions, monsoons are important examples of dynamical complexity[37], driven by land–sea contrasts and complex orography, and are the primary source of precipitation. Meanwhile, mid-latitude weather is dominated by seasonally modulated fronts and the jet stream, the properties of which depend strongly on meridional temperature gradients. As a result, even minor changes of the large-scale spatiotemporal structure of the seasonal cycle can lead to considerable impacts on a regional level, particularly with respect to changes in precipitation.

In this section, we use the eigenfunctions extracted from Indo-Pacific SST to characterize changes in seasonal precipitation in South America over the industrial era. As this region is strongly influenced by ENSO, this trend-driven signal can be possibly concealed in the raw data and hard to extract with traditional data analysis techniques. Here, our strategy is to project historical precipitation fields onto eigenfunctions associated with seasonality and inferred long-term trend in order to isolate the desired signal from ENSO and other nonperiodic modes of variability. In interpreting these results, the reader should keep in mind that, as with any precipitation reanalysis product, 20CR3v3 is subject to uncertainties and systematic biases. See ref.[38] for a comparison of precipitation fields from 20CRv3 and other popular reanalysis products.

Figures 8 and 9 show reconstructions of precipitation fields over South America based on a collection of eigenfunctions that represent the seasonal climatology and the nonstationary trend—see the corresponding spectrum in Supplementary Fig. 1 and Supplementary Table 1. In more detail, in Fig. 8, we show 2D snapshots of reconstructed precipitation fields over South America based on (i) the constant eigenfunction v_1 representing the time-independent climatology; (ii) the complex-conjugate pair $\{v_2, v_3\}$ of annual periodic eigenfunctions (eigenperiod $T_j = 1$ yr), and their semiannual and triannual harmonics, $\{v_4, v_5\}$ and $\{v_9, v_{10}\}$ with eigenperiods $T_j = 1/2$ yr and $T_j = 1/3$ yr, respectively; and (iii) the trend eigenfunction
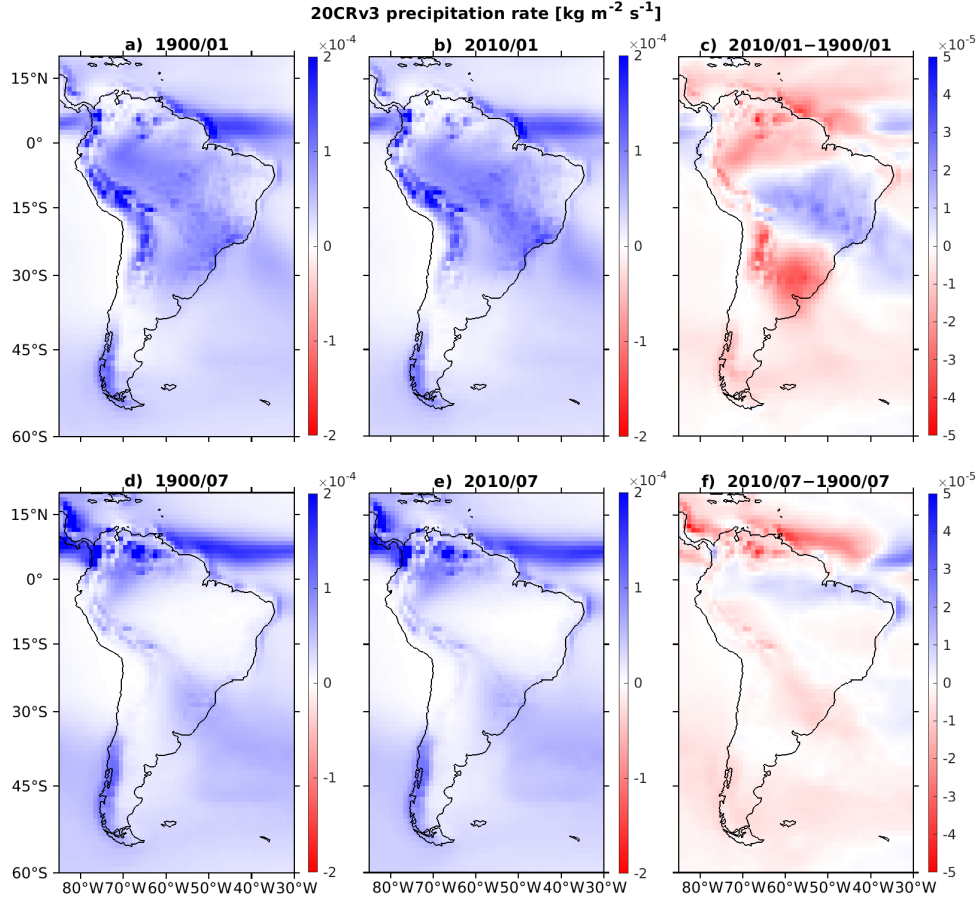
Figure 8. Spatial maps of reconstructed 20CRv3 precipitation rate (in $\text{kg}\,\text{m}^{-2}\,\text{s}^{-1}$) over South America using eigenfunctions representing the global climatology, seasonal cycle, trend, and products between seasonal cycle and trend. Panels (a, d) show reconstructions of precipitation for January 1900 and 2010, respectively. Panels (b, e) show reconstructions for June of the same years, respectively. Panel (c) shows the difference between (b) and (a), and Panel (f) the difference between (e) and (d). The reconstructions in Panels (c, f) provide an estimate of the change in the seasonal cycle of precipitation over the industrial era.

v_6 from Fig. 7 and the complex-conjugate pairs $\{v_7, v_8\}$ and $\{v_{11}, v_{12}\}$ representing products between v_6 and the annual and semiannual pairs.

We interpret the reconstructions based on the union of eigenfunctions from (i), (ii), and (iii) as a time-dependent seasonal cycle associated with the trend represented by eigenfunction v_6. The snapshots in Fig. 8(a, b) are taken in January 1900 and January 2010, respectively; those in Fig. 8(d, e) are taken in July of the same years. Thus, differences between Fig. 8(b) and Fig. 8(a), shown in Fig. 8(c), provide a representation of how South American seasonal precipitation patterns in Austral winter have changed over the past century, and differences between Fig. 8(e) and Fig. 8(d), shown in Fig. 8(f), represent the corresponding changes in Austral summer. The latter, is the active period of the South American Monsoon System (SAMS). In Fig. 9, we show monthly time series of reconstructed precipitation fields sampled in representative locations in South America in 1900 (blue lines) and 2010 (red lines). For the remainder of this section, the terms summer and winter will refer to Austral summer and winter, respectively.

The reconstructed spatial maps and time series show significant changes of the seasonal precipitation
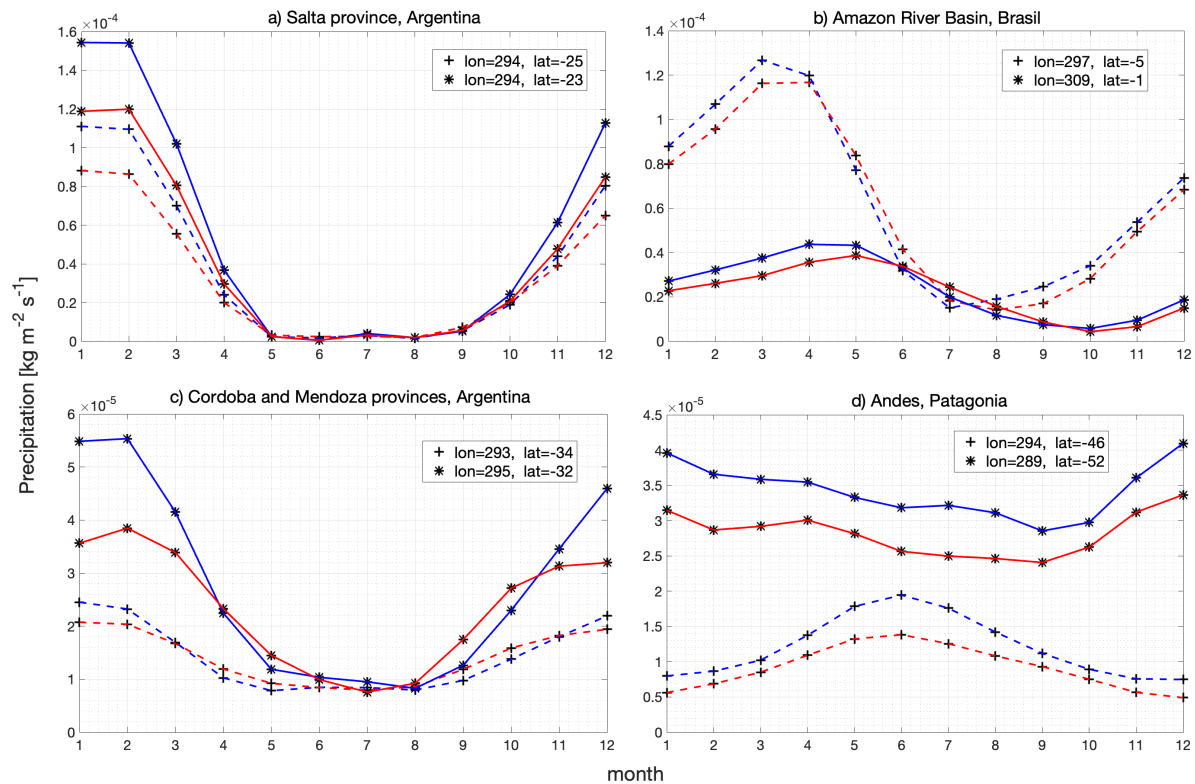
Figure 9. Yearlong evolution of precipitation for four regions in South America that display distinctive change due to trends. Each panel displays reconstructed precipitation time series for two locations within a region (plotted with a dashed line marked with "+", or a solid line marked with "∗" as follows: (a) Salta province in northwest Argentina; (b) equatorial Amazon River basin; (c) Cordoba and Mendoza region, west Argentina; and (d) Patagonia. Blue and red lines depict precipitation reconstructed by the collection of periodic and nonstationary eigenfunctions for year 1900 and 2010, respectively.

cycle in certain regions. First, as can be seen in the region 70°S–10°N and east of 70°W in Fig. 8(c), the northeast parts of South America are characterized by increase of precipitation in the active SAMS season. In contrast, the Amazon river basin drier during winter, as shown in Fig. 8(f). Further south, desert regions east of Andes, such as the Salta province shown in Fig. 9(a), are characterized by absence of precipitation in winter and strong precipitation in summer—the latter, diminishes significantly between 1900 and 2010. Figure 9(c) shows precipitation time series at representative locations encompassing the wine regions of Cordoba and Mendoza province, where drying has been impacting the industry in recent years[39]. Our analysis also shows significant drying of the southern Andes and Patagonia (see Fig. 8), which is in agreement with the recent observational record[40]. A possible explanation for the changes in precipitation seen in Fig. 8 is an equatorward expansion of midlatitude storms, as well as intensification of the Hadley Cell and the South Atlantic Convergence Zone (SACZ).

Quaternary glaciation cycles

The Quaternary geologic period, spanning ∼ 2.6 million years ago (Mya) to the present, is characterized by the presence of glacial–interglacial cycles marked by the growth and decay of continental ice sheets in the northern hemisphere (NH). From the onset of the Quaternary to ∼ 1 Mya, these cycles occurred with a fairly regular periodicity of approximately 41 thousand years (kyr). However, following a transition period

known as the mid-Pleistocene transition (MPT), the NH glaciation cycles switched to a predominantly 100 kyr periodicity and became significantly more asymmetric and temporally irregular[41]. While details of the physical mechanisms underpinning the Quaternary glaciation cycles, including the MPT, remain elusive, they are generally thought to be the outcome of different types of orbital forcings of the Earth's climate system in conjunction with the prevalent atmospheric and geologic conditions such as CO_2 concentration and regolith distribution[42].

More specifically, the dominant orbital forcings of the Earth's climate include (i) orbital precession, with a period of ~ 23 kyr; (ii) axial tilt (obliquity), with a period of ~ 41 kyr; and (ii) orbital eccentricity, with a period of ~ 100 kyr. The response of NH glacial sheets to these forcings over the Quaternary is thought to have been affected by two major factors, namely (i) reduced CO_2 concentration, possibly due to reduced outgassing from volcanoes; and (ii) reduction in NH regolith cover, possibly due to removal by erosion and/or glaciation. In particular, regolith makes ice sheets more mobile and thus more susceptible to orbital forcing. Recent studies[42] have posited that high CO_2 concentration and NH regolith thickness occurring in the early part of the Quaternary are more susceptible to a linear response to the 41 kyr axial tilt forcing, whereas lower CO_2 concentration and NH regolith thickness occurring in the post-MPT period resulted in higher susceptibility to 100 kyr orbital forcings with an associated nonlinear/asymmetric response of NH glacial sheets.

Dataset description

We analyze a scalar time series of $\delta^{18}O$ radioisotope concentration derived from the "LR04" stack of globally distributed benthic $\delta^{18}O$ records of Lisiecki and Raymo[17]. The LR04 dataset spans the past 5.3 Myr and is sampled non-uniformly in time with sampling intervals ranging from 1 kyr over the past 600 kyr to 2 kyr or longer further out in the past. Here, we analyze the past 3 Myr of the LR04 stack. For the purposes of delay embedding, we interpolate the data to a fixed 1 kyr sampling interval using linear interpolation, leading to a $\delta^{18}O$ time series of 3001 samples for analysis depicted in Fig. 10(a). It is clear that the time series exhibits oscillations with a drift in the mean and amplitude, as well as a frequency change around 1 Mya corresponding to the MPT. To examine these features in more detail, Fig. 10(j) displays a continuous wavelet transform (CWT) spectrum of the $\delta^{18}O$ time series where the ~ 40 kyr and ~ 100 kyr glaciation cycles are clearly evident. Note that while the 100 kyr cycle is predominantly active in the post-MPT portion of the time series (i.e., after ~ 1 Mya), the 40 kyr cycle exhibits activity throughout the analysis interval and there is coexistence of the two cycles in the post-MPT record. Our idealized model representing this behavior is Model F′ described in Methods and depicted in Fig. 1.

Glaciation cycles from eigenfunctions

We compute approximate eigenfunctions v_j of the generator by applying the same kernel-based approach as in the SST analysis to the $\delta^{18}O$ time series from the LR04 dataset, shown in Fig. 10(a). Figure 10(b–e) shows time series of the real parts of representative generator eigenfunctions v_j. These eigenfunctions were chosen on the basis of the amplitudes $a_j = |Y_j|$ of the projection coefficients $Y_j = \langle v'_j, h \rangle$ onto the observations h, where $v'_j \in \mathbb{C}^N$ is the dual (biorthonormal) eigenvector to v_j (see Methods), as well as on the basis of their frequency content in relation to known orbital-forcing frequencies. The amplitudes a_j are displayed in Fig. 10(f). In more detail, eigenfunction v_2 in Fig. 10(b) is a real eigenfunction (of zero corresponding eigenfrequency ω_2) that has the largest projection amplitude among all non-constant eigenfunctions of the generator. The eigenfunctions in Figs. 10(c–e) are members of the complex-conjugate pairs that have the second to fourth largest projection amplitudes, respectively. Figure 10(g–i) shows trace plots of these eigenfunctions in the complex plane. Figure 10(k–n) shows CWT spectra of the eigenfunction time series in Fig. 10(b–e), respectively.
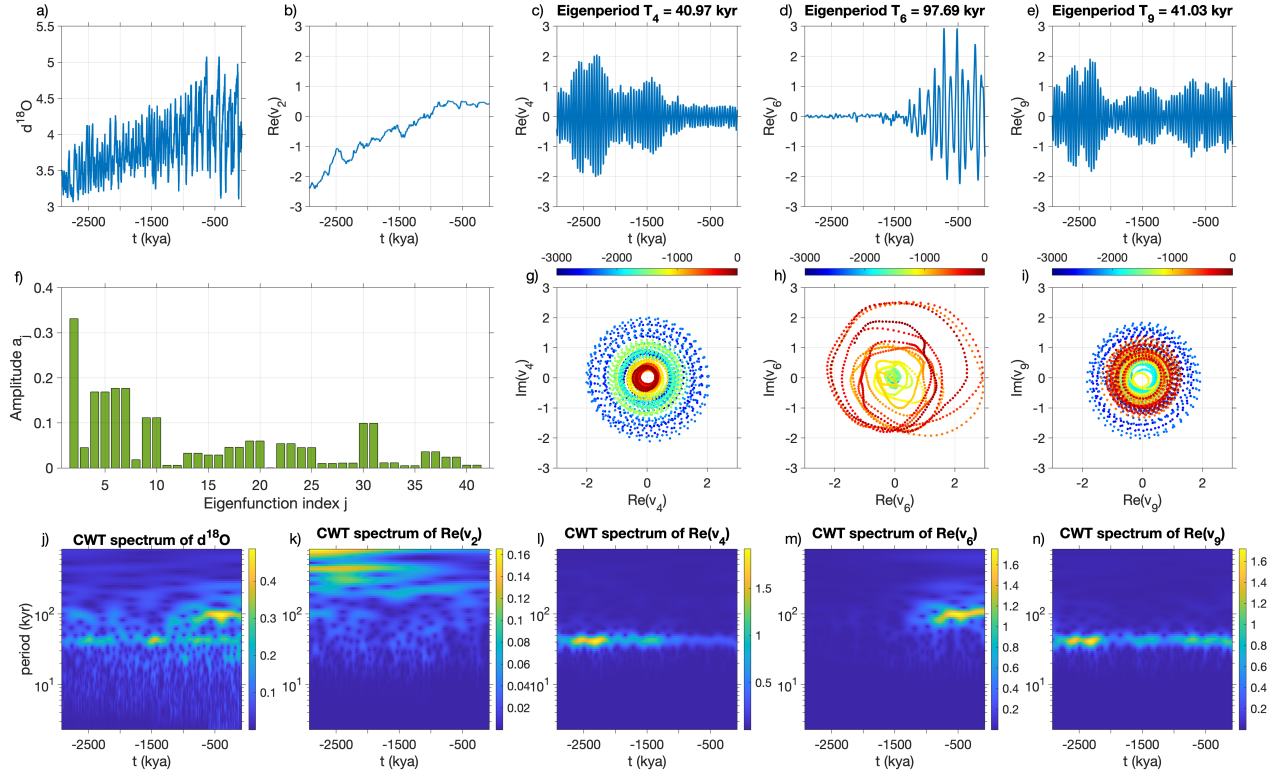
Figure 10. Operator-theoretic analysis of $\delta^{18}O$ data from the LR04 stack over the past 3 Myr. (a) Raw $\delta^{18}O$ time series over the past 3 Myr. (b) Time series of eigenfunction v_2 of the generator representing trend. (c–e) Time series of real parts of oscillatory eigenfunctions v_4, v_6, and v_9, respectively. (f) Moduli a_j of the projection coefficients of the first 40 nonconstant eigenfunctions onto the $\delta^{18}O$ time series. (g–i) Two-dimensional phase space plots of v_4, v_6, and v_9 in the complex plane, colored by time. (j–n) CWT spectra of the $\delta^{18}O$ time series (j) and the time series of eigenfunctions v_2, v_4, v_6, and v_9 (k–n).

It is clear from Fig. 10(b) that eigenvector v_2 represents a secular trend that is consistent with the trend in the mean of the $\delta^{18}O$ concentration signal. Meanwhile, eigenfunctions v_4 (Fig. 10(c, g, l)) and v_6 (Fig. 10(d, h, m)) feature narrowband oscillatory signals which are concentrated in the pre- and post-MPT periods and capture the 40 kyr and 100 kyr glaciation cycles, respectively. The corresponding eigenperiods, $T_4 \approx 41$ kyr and $T_6 \approx 98$ kyr, are also consistent with the dominant pre- and post-MPT periodicities. We also carried out an analogous experiment using an approximation of the transfer operator $\mathscr{L}$ from an embedded $\delta^{18}O$ time series. The leading eigenfunctions of the estimated $\mathscr{L}$ correspond to the trend shown in Fig. 10(b) and to the cycles shown in Figs. 10(c–d); see Supplementary Fig. 3. The corresponding eigenperiods were $T_4 \approx 41$ kyr and $T_6 \approx 99$ kyr.

Besides v_3, v_4, and v_6 (and the complex conjugates of the latter two eigenfunctions, v_5 and v_7, respectively), there are other complex-conjugate pairs in the generator spectrum that project strongly onto the $\delta^{18}O$ time series. The first of these pairs, $\{v_9, v_{10}\}$ has an eigenperiod $T_9 \approx 41$ kyr which is close to the pre-MPT periodicity identified from $\{v_3, v_4\}$, but the amplitude of $\{v_9, v_{10}\}$ is more evenly distributed over the analysis interval, and in particular extends into the post-MPT period (see Fig. 10(e, i, n)). Further down in the spectrum of the generator there eigenfunctions that oscillate at the ~ 23 kyr orbital precession periodicity, as well as eigenfunctions oscillating at intermediate timescales to the 40 kyr and 100 kyr cycles. These eigenfunctions are predominantly active in the post-MPT period, but they

capture less variance than the eigenfunctions shown in Fig. 10 so we do not discuss them further here.

Overall, we find a qualitative difference in the pre- and post-MPT behavior of the dominant oscillatory eigenfunctions: The dominant eigenfunctions exhibiting strong activity in the pre-MPT period, i.e., v_4, v_5, v_9, and v_{10}, have a narrowband frequency spectrum concentrated at approximately $(40 \text{ kyr})^{-1}$. On the other hand, the eigenfunctions v_6, v_7, v_9, and v_{10} (as well as eigenfunctions further down the spectrum), which are active in the post-MPT period exhibit a significantly more diverse range of frequencies, approximately $(100 \text{ kyr})^{-1}$ to $(30 \text{ kyr})^{-1}$. This behavior is consistent with the higher irregularity of NH glaciation cycles known to occur since the MPT.

Discussion

Operator-theoretic techniques designed for analysis of data generated by autonomous dynamical systems have proven to be highly successful in diverse science and engineering applications. Using geometrical arguments, idealized models, and present and past climate data, we have shown that these methods can remain powerful analytical tools even when dealing with systems influenced by time-dependent exogenous factors. In particular, our computations are derived from a *single* observed time series, which is advantageous for the analysis of natural systems such as the Earth's climate system. In such systems there is only one observed history and it is challenging to well-sample ensembles of multiple likely driving conditions.

Central to our approach has been a combination of ideas from time-series delay-embedding geometry, Markov diffusion processes, spectral theory of transfer/Koopman operators, and kernel-based approaches for regularization of dynamical operators of autonomous deterministic systems. We use time delays to embed the observed time series in a higher-dimensional space where changes in the underlying dynamics carry distinct geometrical features (see Fig. 3 (right), Fig. 4 (right), and Fig. 5 (right). By judiciously applying diffusive regularization to transfer and Koopman operators in the delay-embedding space, we compute eigenfunctions that separately encode nonstationary trends and long-lived cycles, and which are associated with the diffusion and drift components, respectively, of the regularized operators. In addition, spectral decomposition of the regularized operators yields product eigenfunctions that capture the modulation of the system's fundamental cycles by the nonstationary trends.

We illustrated the above ideas through idealized models that were chosen as surrogates of nonautonomous dynamics in two challenging real-world problems: Climate change occurring over the industrial era and the mid-Pleistocene transition (MPT) of Quaternary glaciation cycles. We demonstrated that eigenfunctions of transfer operators can successfully recover trends in systems undergoing drifts in the mean and amplitude of their oscillatory dynamics; (Models M and A, respectively). One of our main theoretical results (Lemma 1) shows that low-dimensional delay embedding successfully delineates non-autonomous frequency switching in systems with oscillatory dynamics; (Model F; see Fig. 1 and Fig. 6).

We then demonstrated the utility of our methods directly on Indo-Pacific SST and δ^{18}O radioisotope concentration data. The Indo-Pacific SST analysis yielded eigenfunctions that provide a nonparametric representation of climate change trends. In addition, these eigenfunctions have associated families of product modes capturing the response of the seasonal cycle to the trend. Using these eigenfunction families, we reconstructed spatiotemporal patterns revealing significant regional changes in South American seasonal precipitation, which we attributed to meridional shifts of the South American Monsoon. Meanwhile, the δ^{18}O analysis yielded eigenfunctions representing the long-term trend of δ^{18}O concentration over the past 3 million years, as well as the fundamental 40 kyr and 100 kyr glaciation cycles occurring before and after the MPT, respectively. One of the key findings of this analysis was the presence of multiple coexisting cycles in the post-MPT period ($\sim$ 1 Mya to the present), which could help explain the irregularity of

glaciation cycles in that period.

In conclusion, the theory and results described in this paper demonstrate the ability of autonomous operator-theoretic techniques to extract trends and cycles from certain classes of non-autonomous systems. Importantly, these autonomous methods use information from a single time series, enabling them to be applied in many natural science domains such as climate dynamics where repeated experiments are impossible. We envisage that our approach will stimulate further research and applications at the interface between autonomous and non-autonomous methodologies for data-driven analysis of dynamical systems, and help to guide the possible combination of these distinct techniques.

Methods

Model F′: Switching between two coexisting oscillation frequencies

Model F described dynamics switching between two rotation frequencies on two halves of a cylinder, where the phase around the cylinder was read off by a fixed observation function. One could alternatively move the nonstationarity out of the dynamics and into the observation function; we call this alternative "Model F′". The dynamics $T : [0,1] \times S^1 \times S^1 \circlearrowleft$ of Model F′ occur on an enlarged phase space—a solid 2-torus $[0,1] \times S^1 \times S^1$, see Fig. 1 (Center Right)—to allow for two frequencies to always exist, while the observation function $h : [0,1] \times S^1 \times S^1 \mapsto \mathbb{R}$ predominantly records one frequency or the other. Explicitly, we have

$$T(x,\theta) = (f(x), \theta_1 + \alpha_1, \theta_2 + \alpha_2), \tag{6}$$

and

$$h(x, \theta_1, \theta_2) = w(x)\cos(2\pi\theta_1) + (1 - w(x))\cos(2\pi\theta_2). \tag{7}$$

Proof of Lemma 1

For $0 < \beta \leq \pi/2$ the elliptical images $e_\beta \subset \mathbb{R}^3$ of a unit circle under γ_β lie in the plane p_β spanned by $[1, \cos(\beta), \cos(2\beta)]$ and $[0, -\sin(\beta), -\sin(2\beta)]$. As β varies, this family of planes always contain the fixed vector $[1, 0, -1]$. One may compute that the vector $[\sin(2\beta), 2\sin(\beta), \sin(2\beta)]$ is orthogonal to $[1, 0, -1]$, and that together they span p_β. Note that the vectors $[\sin(2\beta), 2\sin(\beta), \sin(2\beta)]$ are distinct for distinct $0 < \beta \leq \pi/2$. This means that for $\beta \neq \beta' \in (0, \pi/2]$ the only intersection of p_β and $p_{\beta'}$ (and therefore the only possible intersection of e_β and $e_{\beta'}$) is along the vector $[1, 0, -1]$.

The behavior of the e_β is as follows. For $\beta = 0$, one obtains a degenerate ellipse (a line segment) passing through the origin in the direction $[1, 1, 1]$ (this is the $\beta \to 0$ limiting direction of $[\sin(2\beta), 2\sin(\beta), \sin(2\beta)]$). For $0 < \beta \leq \pi/2$ one obtains an ellipse with one axis in the direction $[\sin(2\beta), 2\sin(\beta), \sin(2\beta)]$ of length $\sqrt{2 + \cos(2\beta)}$ and the other axis in the direction $[1, 0, -1]$ of length $\sqrt{1 - \cos(2\beta)}$. These two lengths are the singular values of the transformation Φ. As the planes p_β (and the ellipses e_β contained in them) pivot about the fixed vector $[1, 0, -1]$, the length of their axis in this direction increases monotonically from $\beta = 0$ to $\beta = \pi/2$. This axis length increase combined with the pivoting about a common axis direction implies that they are disjoint for $0 < \beta \neq \beta' \leq \pi/2$.

One can verify that the product of the above two singular values of Φ has a unique maximum in the range $\beta \in [0, \pi/2]$ at $\beta = \pi/3$, where this product has the value 1.5. The angle $\beta = \pi/3$ is also the unique angle in $[0, \pi/2]$ where the singular values coincide, and therefore also the unique angle for which the ellipse e_β is a circle. □

Reconstruction of observables by projection onto eigenfunctions

Let $v_i \in \mathbb{C}^N$ denote an eigenvector onto which we wish to project, and let $v_i' \in \mathbb{C}^N$ denote the corresponding eigenvector of the adjoint transfer operator $P^\top$ (or the adjoint generator), where we normalize so that $v_i'^\dagger v_i = 1$. Here, $\dagger$ is the complex-conjugate transpose. Because $v_i'^\dagger v_j = 0$ for $i \neq j$, the standard rank-1 projection matrix $\Pi_i := v_i v_i'^\dagger$ has range $\text{span}\{v_i\}$ and nullspace $\text{span}\{v_j\}_{j \neq i}$. We may now project an arbitrary *scalar-valued* time series $\{y_n\}_{n=1}^N$ represented by the N-vector y onto v_i by acting on y with matrix multiplication by Π_i according to $(\Pi_i y)_m = \sum_{n=1}^N \Pi_{mn} y_n = v_{i,m} \cdot (\sum_{n=1}^N \overline{v_{i,n}'} y_n)$. To project *vector-valued* time series (e.g., SST images) $\{Y_n\}_{n=1}^N$ where each $Y_n \in \mathbb{R}^d$, we act on $Y \in \mathbb{R}^{N \times d}$ in an analogous way, applying the projection Π_i componentwise in $\mathbb{R}^d$: $(\Pi_n(Y))_m := v_{i,m} \cdot (\sum_{n=1}^N \overline{v_{n,j}'} Y_n) \in \mathbb{C}^d$. In addition, given a collection $\{v_{i_1}, \ldots, v_{i_r}\}$ of distinct eigenvectors, we may project onto the r-dimensional subspace $\text{span}\{v_{i_1}, \ldots v_{i_r}\}$ by forming the rank-r projection matrix $\Pi = \sum_{j=1}^r \Pi_{i_j}$ and acting with it on Y componentwise: $(\Pi(Y))_m = \sum_{j=1}^r (\Pi_{i_j}(Y))_m = \sum_{j=1}^r v_{i_j,m} \cdot (\sum_{n=1}^N \overline{v_{i_j,n}'} Y_n)$. If the collection $\{v_{i_1}, \ldots, v_{i_r}\}$ consists of real eigenvectors and/or complex-conjugate pairs, then $\Pi(Y)$ is real. If we employ Takens embedding on the time series $\{Y_n\}$ in order to improve state estimation, the above action of Π is again applied componentwise to the delay vectors formed from concatenations of various Y_n. See Methods in ref.[14], or ref.[36], for further details.

Indo-Pacific SST calculations

We analyze a time series $h_1, \ldots, h_{\tilde{N}}$ of monthly-averaged Indo-Pacific SST, where h_1 is the snapshot for January 1891 and $h_{\tilde{N}}$ with $\tilde{N} = 1548$ is the snapshot for December 2019. Each analyzed SST snapshot h_t contains $d = 4868$ gridpoints, i.e., it is considered as a point in $\mathbb{R}^{4868}$. Using this data, we compute data-driven approximations of the transfer operator and the generator of the Koopman/transfer operator groups using the methods described in ref.[14]. Results from the generator calculations are discussed in the main text. The transfer operator results are broadly consistent with those from the generator and are described in the Supplementary Information. A full listing of the parameters used in our experiments is included in Supplementary Table 1.

Generator approximation

For computation of the eigenvectors of the generator we apply Takens delay embedding to the snapshots with $Q - 1 = 47$ lags of duration $\ell = 1$ month. We thus obtain an embedding window length of 4 yr and corresponding SST "videos" of dimension $dQ = 233,664$. This choice of embedding parameters was previously found[14] to provide adequate representation of annual and interannual processes such as the seasonal cycle and ENSO, respectively, as well as longer-term processes such as climate change trends and Pacific decadal variability. We use the delay-embedded data to build a kernel matrix of size $N \times N$, $N = \tilde{N} - Q + 1 = 1501$, whose top $L = 401$ eigenvectors provide a data-driven basis of observables for representing the generator as an $L \times L$ matrix with respect to this basis. The result is a collection of eigenvectors $v_1, v_2, \ldots, v_L \in \mathbb{C}^N$ and corresponding eigenvalues $\gamma_1, \gamma_2, \ldots, \gamma_L \in \mathbb{C}$, where $-\operatorname{Re}\gamma_i$ represents decay rate and $\operatorname{Im}\omega_i$ represents oscillatory frequency. We order the eigenpairs (γ_i, v_i) in order of increasing decay rate (i.e., decreasing $\operatorname{Re}\gamma_i$). We note that our numerical results are not particularly sensitive on the choice of Q and L, and qualitatively similar results can be obtained for Q in the range 24–120 and L in the range 200–500.

Transfer operator approximation

For the construction of the transition matrix P we use a single lag, setting $Q = 2$ to minimize the sparsity of the data, producing embedded data points in $\mathbb{R}^{9736}$. We use a lag duration of $\ell = 12$ months, which is about one quarter of the average period of the ENSO cycle. To reduce the effect of noise, we step forward

$s = 6$ months, and we slightly reduce the neighborhood size to $K = 5$ to obtain more accurate estimates of the ENSO cycle. Supplementary Fig. 2 displays the leading nontrivial real eigenvector (corresponding to eigenvalue $\lambda_2 = 0.4135$). This second eigenvalue is relatively far from unity because of the sparsity of the high-dimensional data; nevertheless the corresponding eigenvector is consistent with a qualitative description of the warming trend over the last 150 years, as illustrated in Supplementary Fig. 2 through comparisons with global SST and global SAT.

δ^{18}O radioisotope concentration calculations

The time series of δ^{18}O concentration derived by interpolation of the LR04 stack is scalar-valued ($d = 1$), and consist of $\tilde{N} = 3001$ samples taken every 1 kyr over the last 3 Myr. We compute approximate eigenfunctions of the transfer operator and the generator using the same methods as in the Indo-Pacific SST experiments. A full listing of the parameters is provided in Supplementary Table 3.

Generator approximation

We use a delay embedding window spanning 150 kyr (i.e., $Q = 150$ and $\ell = 1$ kyr). This embedding window was chosen on the basis of being comparable to the ~ 100 kyr characteristic timescale of the post-MPT glaciation cycles, though our results are not too sensitive on this choice. After embedding, the number of samples available for analysis is $N = \tilde{N} - Q + 1 = 2851$. We use the leading $L = 81$ eigenvectors of the associated $N \times N$ kernel matrix to approximate the generator as in the Indo-Pacific SST analysis.

Transfer operator approximation

We embed the relatively noisy scalar signal h_t in five dimensions so as to reduce false neighbors. We use a fixed lag $\ell = 10$ kyr (10 sampling intervals) chosen approximately according to the considerations following Lemma 1. To further reduce the effect of noise we step forward 7000 years at a time ($s = 7$ sampling intervals) when constructing the transition matrix P; $K = 7$ nearest neighbors are used to set the variable bandwidth. The eigenfunction corresponding to the second eigenvalue extracts the δ^{18}O trend in the mean of the signal; see Supplementary Fig. 3 for a comparison between the original signal and the mean trend. The two leading complex eigenvectors extract and separate the two dominant frequency regimes in the δ^{18}O signal; see Supplementary Note 2 and Supplementary Fig. 3. The corresponding complex eigenvalues estimate cycle lengths of 98,640 and 40,775 yr, which match well with the accepted periods either side of the MPT. Thus the eigenvectors of the transfer operator have separated the trend in the mean of the δ^{18}O time series from the oscillatory components. Further, the complex eigenvectors have separated and identified the two dominant frequencies, including indicating when each frequency is present through the amplitude of the eigenvectors.

Acknowledgments

Author Contributions Statement

G.F. and D.G. designed and performed the theoretical study and numerical experiments on idealized non-autonomous models. G.F., D.G., and J.S. designed the study on industrial-era climate dynamics, performed the associated operator computations and interpreted the results. D.G. and J.S. designed the study on glaciation cycles. E.L. prepared the δ^{18}O dataset. G.F., D.G., and E.L. performed the associated operator computations and interpreted the results. G.F. and D.G. wrote the paper. All authors read and approved the final manuscript.

Competing Interests

The authors declare that they have no competing interests.

Data Availability

The ERSSTv4, NCEP, and 20CRv3 reanalysis data are available at the National Centers for Environmental Information repositories, under accession codes https://www.ncdc.noaa.gov/data-access/marineocean-data/extended-reconstructed-sea-surface-temperature-ersst-v4 and https://psl.noaa.gov/data/gridded/data.ncep.reanalysis.html, https://www.psl.noaa.gov/data/gridded/data.20thC_ReanV3.html, respectively. The δ^{18}O concentration data from the LR04 stack are available at the URLs https://lorraine-lisiecki.com/stack.html. The processed data are available from the corresponding author on reasonable request.

Code Availability

MATLAB code implementing transfer operator calculations for Models M, A, and F, as well as the ENSO and ice-core data is available at https://github.com/gfroyland/Trends. MATLAB code implementing the numerical approximation of the generator employed in the paper is available at https://dg227.github.io/NLSA/.

References

1. Dellnitz, M., Froyland, G. & Sertl, S. On the isolated spectrum of the Perron–Frobenius operator. *Nonlinearity* **13**, 1171–1188, DOI: 10.1088/0951-7715/13/4/310 (2000).

2. Mezić, I. Spectral properties of dynamical systems, model reduction and decompositions. *Nonlinear Dyn.* **41**, 309–325, DOI: 10.1007/s11071-005-2824-x (2005).

3. Berry, T., Giannakis, D. & Harlim, J. Bridging data science and dynamical systems theory. *Notices Amer. Math. Soc.* **67**, 1336–1349, DOI: 10.1090/noti2151 (2020).

4. Budrene, E. O. & Berg, H. C. Dynamics of formation of symmetrical patterns by chemotactic bacteria. *Nature* **376**, 49–53, DOI: 10.1038/376049a0 (1995).

5. Vicsek, T. & Zafeiris, A. Collective motion. *Phys. Rep.* **517**, 71–140, DOI: 10.1016/j.physrep.2012.03.004 (2012).

6. Deco, G. *et al.* Awakening: Predicting external stimulation to force transitions between different brain states. *Proc. Natl. Acad. Sci.* **116**, 18088–18097, DOI: 10.1073/pnas.1905534116 (2019).

7. Favela, L. H. Dynamical systems theory in cognitive science and neuroscience. *Philos. Compass* **15**, DOI: 10.1111/phc3.12695 (2020).

8. Pandey, A., Scheel, J. D. & Schumacher, J. Turbulent superstructures in Rayleigh-Bénard convection. *Nat. Comm.* **9**, 2118, DOI: 10.1038/s41467-018-04478-0 (2018).

9. Sreenivasan, K. R. Turbulent mixing: A perspective. *Proc. Natl. Acad. Sci.* **116**, 18175–18183, DOI: 10.1073/pnas.1800463115 (2018).

10. Cai, W. *et al.* ENSO and greenhouse warming. *Nat. Clim. Chang.* **5**, 849–859, DOI: 10.1038/nclimate2743 (2015).

11. Ghil, M. & Lucarini, V. The physics of climate variability and climate change. *Rev. Mod. Phys.* **92**, DOI: 10.1103/RevModPhys.92.035002 (2020).

12. Froyland, G., Lloyd, S. & Quas, A. Coherent structures and isolated spectrum for Perron–Frobenius cocycles. *Ergod. Theory Dyn. Syst.* **30**, 729–756, DOI: 10.1017/S0143385709000339 (2010).

13. Froyland, G., Lloyd, S. & Santitissadeekorn, N. Coherent sets for nonautonomous dynamical systems. *Phys. D* **239**, 1527–1541, DOI: doi:10.1016/j.physd.2010.03.009 (2010).

14. Froyland, G., Giannakis, D., Lintner, B., Pike, M. & Slawinska, J. Spectral analysis of climate dynamics with operator-theoretic approaches. *Nat. Commun.* **12**, DOI: 10.1038/s41467-021-26357-x (2021).

15. Timmermann, A. *et al.* El Niño–Southern Oscillation complexity. *Nature* **559**, 535–545, DOI: 10.1038/s41586-018-0252-6 (2018).

16. Lisiecki, L. E. & Raymo, M. E. Plio–Pleistocene climate evolution: Trends and transitions in glacial cycle dynamics. *Quat. Sci. Rev.* **26**, 56–69, DOI: 10.1016/j.quascirev.2006.09.005 (2007).

17. Lisiecki, L. E. & Raymo, M. E. A Pliocene–Pleistocene stack of 57 globally distributed benthic $\delta^{18}O$ records. *Paleoceanography* **26**, 56–69, DOI: 10.1029/2004PA001071 (2007).

18. Packard, N. H. *et al.* Geometry from a time series. *Phys. Rev. Lett.* **45**, 712–716, DOI: 10.1103/physrevlett.45.712 (1980).

19. Broomhead, D. S. & King, G. P. Extracting qualitative dynamics from experimental data. *Phys. D* **20**, 217–236, DOI: 10.1016/0167-2789(86)90031-x (1986).

20. Vautard, R. & Ghil, M. Singular spectrum analysis in nonlinear dynamics, with applications to paleoclimatic time series. *Phys. D* **35**, 395–424, DOI: 10.1016/0167-2789(89)90077-8 (1989).

21. Takens, F. Detecting strange attractors in turbulence. In *Dynamical Systems and Turbulence*, vol. 898 of *Lecture Notes in Mathematics*, 366–381, DOI: 10.1007/bfb0091924 (Springer, Berlin, 1981).

22. Sauer, T., Yorke, J. A. & Casdagli, M. Embedology. *J. Stat. Phys.* **65**, 579–616, DOI: 10.1007/bf01053745 (1991).

23. Robinson, J. C. A topological delay embedding theorem for infinite-dimensional dynamical systems. *Nonlinearity* **18**, 2135–2143, DOI: 10.1088/0951-7715/18/5/013 (2005).

24. Stark, J. Delay embeddings for forced systems. I. Deterministic forcing. *J. Nonlinear Sci.* **9**, 255–332, DOI: 10.1007/s003329900072 (1999).

25. C., R. J. A topological time-delay embedding theorem for infinite-dimensional cocycle dynamical systems. *Discret. Contin. Dyn. Syst. Ser. B* **9**, 731–741, DOI: 10.3934/dcdsb.2008.9.731 (2008).

26. Marotzke, J. & Forster, P. M. Forcing, feedback and internal variability in global temperature trends. *Nature* **517**, 565–570, DOI: 10.1038/nature14117 (2015).

27. Hu, S. & Fedorov, A. V. The extreme el Niño of 2015–2016 and the end of global warming hiatus. *Geophys. Res. Lett.* **44**, 3816–3824, DOI: 10.1002/2017GL072908 (2017).

28. Maher, N., Lehner, F. & Marotzke, J. Quantifying the role of internal variability in the temperature we expect to observe in the coming decades. *Environ. Res. Lett.* **15**, DOI: 10.1088/1748-9326/ab7d02 (2020).

29. Karl, T. R. *et al.* Possible artifacts of data biases in the recent global surface warming hiatus. *Science* **348**, 1469–1472, DOI: 10.1126/science.aaa5632 (2015).

30. Fyfe, J. C. *et al.* Making sense of the early-2000s warming slowdown. *Nat. Clim. Chang.* **6**, 224–228, DOI: 10.1038/nclimate2938 (2016).

31. Stuecker, M. F., Jin, F. F. & Timmermann, A. El Niño–Southern Oscillation frequency cascade. *Proc. Natl. Acad. Sci.* **112**, 13490–13495, DOI: 10.1073/pnas.1508622112 (2015).

32. Lenssen, N. J. L. *et al.* Improvements in the GISTEMP uncertainty model. *J. Geophys. Res. Atmos.* **124**, 6307–6326, DOI: 10.1029/2018JD029522 (2019).

33. Huang, B. *et al.* Extended Reconstructed Sea Surface Temperature version 4 (ERSST.v4): Part I. Upgrades and intercomparisons. *J. Clim.* **28**, 911–930, DOI: 10.1175/JCLI-D-14-00006.1 (2014).

34. Zhang, H.-M., Huang, B., Lawrimore, J. H., Menne, M. J. & Smith, T. M. NOAA global surface temperature dataset (NOAAGlobalTemp), version 5.0, DOI: 10.25921/9qth-2p70 (2019). Accessed April 27, 2023.

35. Slivinski, L. C. *et al.* Towards a more reliable historical reanalyis: Improvements for version 3 of the Twentieth Century Reanalysis system. *Quart. J. Roy. Meteor. Soc.* **145**, 2876–2908, DOI: 10.1002/qj.3598 (2019).

36. Ghil, M. *et al.* Advanced spectral methods for climatic time series. *Rev. Geophys.* **40**, DOI: 10.1029/2000rg000092 (2002).

37. Webster, P. J. *et al.* Monsoons: Processes, predictability, and the prospects for prediction. *J. Geophys. Res. Ocean.* **103**, 14451–14510, DOI: 10.1029/97JC02719 (1998).

38. Slivinski, L. C. *et al.* An evaluation of the performance of the Twentieth Century Reanalysis Version 3. *J. Clim.* **34**, 1417–1438, DOI: 10.1175/JCLI-D-20-0505.1 (2021).

39. Rivera, J. A., Otta, S., Lauro, C. & Zazulie, N. A decade of hydrological drought in central-western Argentina. *Front. Water* **3**, DOI: 10.3389/frwa.2021.640544 (2021).

40. Barros, V. R. *et al.* Climate change in Argentina: Trends, projections, impacts, and adaptation. *Wiley Interdiscip. Rev. Clim. Chang.* **6**, 151–169, DOI: 10.1002/wcc.316 (2015).

41. Clark, P. U. *et al.* The middle Pleistocene transition: Characteristics, mechanisms, and implications for long-term changes in atmospheric pCO_2. *Quat. Sci. Rev.* **25**, 3150–3184, DOI: 10.1016/j.quascirev.2006.07.008 (2006).

42. Willeit, M., Ganopolski, A., Calov, R. & Brovkin, V. Mid-Pleistocene transition in glacial cycles explained by declining CO_2 and regolith removal. *Sci. Adv.* **5**, DOI: 0.1126/sciadv.aav7337 (2019).

Revealing trends and persistent cycles of non-autonomous systems with operator-theoretic techniques: Applications to past and present climate dynamics

Gary Froyland[1,*]**, Dimitrios Giannakis**[2,3]**, Edoardo Luna**[4]**, and Joanna Slawinska**[2]

[1]School of Mathematics and Statistics, University of New South Wales, Sydney, NSW 2052, Australia
[2]Department of Mathematics, Dartmouth College, Hanover, NH 03755, USA
[3]Department of Physics and Astronomy, Dartmouth College, Hanover, NH 03755, USA
[4]Department of Physics, University of Texas at Austin, Austin, TX 78712, USA
[*]g.froyland@unsw.edu.au

SUPPLEMENTARY INFORMATION

The contents of the Supplementary Information are as follows:

- Eigenvalue spectrum of the generator extracted from Indo-Pacific SST (Supplementary Fig. 1 and Supplementary Table 2).

- SST trend from transfer operator calculations (Supplementary Note 1, Supplementary Fig. 2).

- δ^{18}O concentration trend and frequency analysis from transfer operator calculations (Supplementary Note 2, Supplementary Fig. 3).

- Details of data and operator parameters (Supplementary Table 3).

Supplementary Note 1. SST trend from transfer operator calculations

We construct the transfer operator for the Indo-Pacific SST analysis as described in the "Indo-Pacific SST calculations" section in Methods. Supplementary Fig. 2 (left) displays the leading nontrivial real eigenvector – corresponding to eigenvalue $\lambda_2 = 0.4135$ – in blue, and global SST in green. Similarly, Supplementary Fig. 2 (right) compares the same eigenvector with global SAT.

In both cases, the warming trend extracted by the transfer operator from Indo-Pacific SST fields closely matches the global SST and SAT time series.

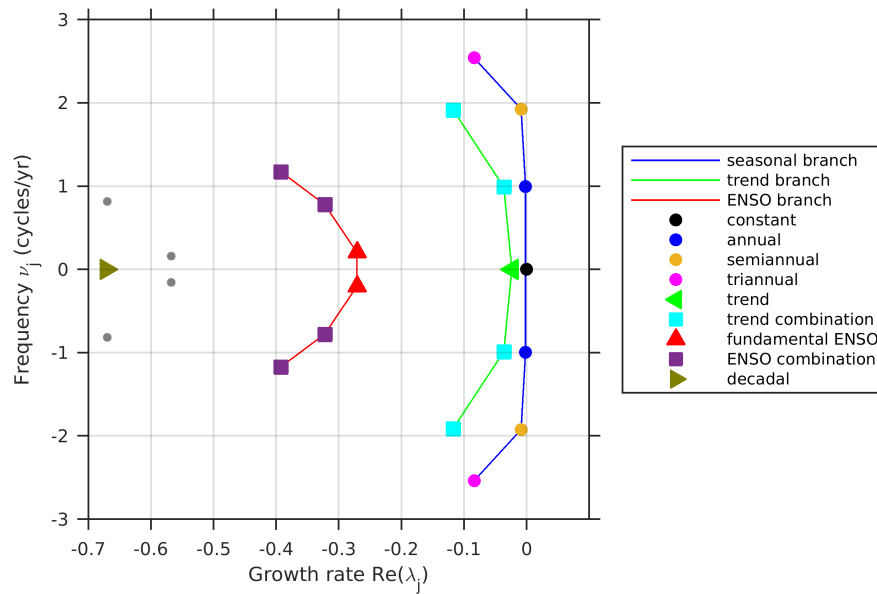## Supplementary Note 2. δ^{18}O analysis using transfer operators

We construct the transfer operator for the δ^{18}O analysis as described in the "δ^{18}O radioisotope concentration calculations" section in Methods. Supplementary Fig. 3 (left) displays the second eigenvector of the transfer operator approximation (corresponding to eigenvalue $\lambda_2 = 0.9632$), which is qualitatively consistent with the trend in the mean of the signal. The right two panels of Supplementary Fig. 3 show the real parts of two distinct complex eigenvectors. These are the leading two complex-conjugate pairs, and have eigenvalues $\lambda_4 = 0.7639 + 0.3651i$ and $\lambda_6 = 0.3869 + 0.7216i$. From the arguments of these eigenvalues (multiplied by 5 because we are stepping forward 5 sampling intervals) we obtain corresponding

cycle periods of 98.64 and 40.78 Myr, which match the accepted distinct MPT cycle periods very well. Importantly, we note that the amplitude of the oscillations of the eigenvectors in the two rightmost panels of Supplementary Fig. 3 are largest in the time domain corresponding to when the oscillation is present.
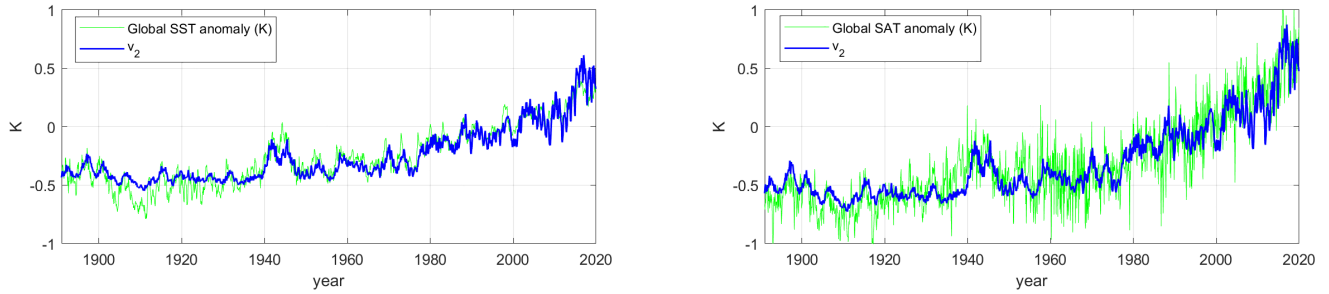
Thus in summary, the eigenvectors of the transfer operator have separated the trend in the mean of the $\delta^{18}O$ time series from the oscillatory components. Further, the complex eigenvectors have separated and identified the two dominant frequencies, including indicating when each frequency is present through the amplitude of the eigenvectors. The results in the first row of Fig. 10 are also consistent with Supplementary Fig. 3.
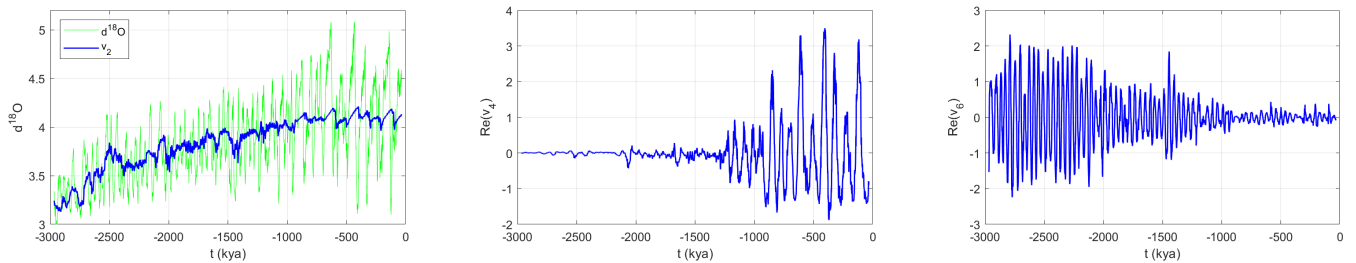
References

1. Froyland, G., Giannakis, D., Lintner, B., Pike, M. & Slawinska, J. Spectral analysis of climate dynamics with operator-theoretic approaches. *Nat. Commun.* **12**, DOI: 10.1038/s41467-021-26357-x (2021).

Supplementary Figure 1. Leading generator eigenvalues λ_j computed from monthly-averaged Indo-Pacific SST data from ERSSTv4 over the period January 1891 to December 2019. The vertical and horizontal axes show the frequency $\text{Im}(\lambda_j)/(2\pi)$ and growth rate, $\text{Re}(\lambda_j)$, respectively. Note that complex eigenvalues occur in complex-conjugate pairs as appropriate for describing oscillatory signals at the corresponding eigenfrequencies. Moreover, negative values of $\text{Re}(\lambda_j)$ correspond to decay. Following Fig. 3 in ref.[1] – which used Indo-Pacific SST time series from January 1970 to February 2020 – we group the eigenvalues into branches associated with seasonal (periodic), trend, ENSO, and decadal eigenfunctions. Lines connecting eigenvalues serve as visual guides for these spectral branches. A listing of the parameters employed for generator approximation can be found in Supplementary Table 1.

Supplementary Figure 2. *Left:* The second eigenvector of the transfer operator (the first nontrivial real eigenvector) shown in blue captures the trend in the Indo-Pacific SST signal. The globally averaged SST anomaly is shown in green. *Right:* The same second eigenvector is shown in blue. The globally averaged SAT anomaly is shown in green. In each case, the eigenvector has been affinely scaled to convert its arbitrary units to Kelvin.

Supplementary Figure 3. *Left:* The second eigenvector (the first nontrivial real eigenvector) shown in blue captures the drift in the mean of the original $\delta^{18}O$ signal in green. The eigenvector has been affinely scaled to convert its arbitrary units to $\delta^{18}O$ concentration. *Center:* real part of the fifth eigenvector (from the first nontrivial complex eigenvector pair) displays an oscillation period of 98,640 years, which corresponds to oscillations in the $\delta^{18}O$ time series over the most recent 1.5 million years. *Right:* The real part of the seventh eigenvector (from the second nontrivial complex eigenvector pair) displays an oscillation period of 40,775 years, which corresponds to oscillations in the $\delta^{18}O$ time series from 3 million to 2 million years ago.

Supplementary Table 1. Dataset attributes and numerical parameter values for the analyses of Indo-Pacific SST from ERSSTv4. See Methods in ref.[1] for further details on the generator approximation parameters.

Dataset Attributes	
Analysis date range	Jan 1891 – Dec 2019
Climatology date range[a]	Jan 1971 – Dec 2000
Sampling interval Δt	1 month
Number of snapshots N	1548
SST analysis domain	28°E–70°W, 60°S–20°N
Nominal resolution	2°
Number of gridpoints d	4868

Generator Approximation	
Number of delays Q	48
Timesteps between delays ℓ	1
Kernel bandwidth parameter γ	33
Cone kernel parameter ζ	0.995
Number of kernel eigenfunctions L	400
Generator regularization parameter ε	0.001

Transfer Operator Approximation	
Number of delays Q	2
Timesteps between delays ℓ	12
Number of forward steps s	6
Number of nearest neighbors K	5

[a]Used to compute SST and SAT anomalies.

Supplementary Table 2. Eigenfrequencies and eigenperiods corresponding to the leading 25 generator eigenfunctions extracted from Indo-Pacific ERSSTv4 data. See Methods in ref.[1] for further details on the generator approximation parameters.

	Frequency (yr^{-1})	Period (yr)	Type
v_1	0.000	∞	constant
v_2	0.995	1.005	annual
v_3	-0.995	-1.005	annual
v_4	1.925	0.520	semiannual
v_5	-1.925	-0.520	semiannual
v_6	0.000	∞	trend
v_7	0.988	1.012	trend combination
v_8	-0.988	-1.012	trend combination
v_9	2.539	0.394	triannual
v_{10}	-2.539	-0.394	triannual
v_{11}	1.913	0.523	trend combination
v_{12}	-1.913	-0.523	trend combination
v_{13}	0.204	4.910	ENSO
v_{14}	-0.204	-4.910	ENSO
v_{15}	0.779	1.284	ENSO combination
v_{16}	-0.779	-1.284	ENSO combination
v_{17}	1.172	0.853	ENSO combination
v_{18}	-1.172	-0.853	ENSO combination
v_{19}	0.157	6.386	
v_{20}	-0.157	-6.386	
v_{21}	0.817	1.225	
v_{22}	-0.817	-1.225	
v_{23}	0.000	∞	decadal
v_{24}	1.727	0.579	
v_{25}	-1.727	-0.579	

Supplementary Table 3. Dataset attributes and numerical parameter values for the analyses of $\delta^{18}O$ concentration data from the LR04 stack.

Dataset Attributes	
Analysis date range	3 Mya – present
Sampling interval Δt	1 kyr
Number of snapshots N	3001

Generator approximation	
Number of lags Q	150
Timesteps between lags ℓ	1
Kernel bandwidth parameter γ	0.216
Cone kernel parameter ζ	0
Number of kernel eigenfunctions L	81
Generator regularization parameter ε	0.001

Transfer operator approximation	
Number of delays Q	5
Timesteps between delays ℓ	10
Number of forward steps s	7
Number of nearest neighbors K	7